

2

BRL

JOHN D. POWELL
ALEXANDER E. ZIELINSKI

JUNE 1992

DTIC
ELECTRONIC
JUN 11 1992

APPROVED FOR PUBLIC RELEASE; DISTRIBUTION IS UNLIMITED.

U.S. ARMY LABORATORY COMMAND

BALLISTIC RESEARCH LABORATORY
ABERDEEN PROVING GROUND, MARYLAND

92-15201

[illegible]

**Best
Available
Copy**

NOTICES

Destroy this report when it is no longer needed. DO NOT return it to the originator.

Additional copies of this report may be obtained from the National Technical Information Service, U.S. Department of Commerce, 5285 Port Royal Road, Springfield, VA 22161.

The findings of this report are not to be construed as an official Department of the Army position, unless so designated by other authorized documents.

The use of trade names or manufacturers' names in this report does not constitute indorsement of any commercial product.

REPORT DOCUMENTATION PAGE			Form Approved OMB No 0704-0188	
<small>Public reporting burden for this collection of information is estimated to average 1 hour per response, including the time for reviewing instructions, searching existing data sources, gathering and maintaining the data needed, and completing and reviewing the collection of information. Send comments regarding this burden estimate or any other aspect of this collection of information, including suggestions for reducing this burden, to Washington Headquarters Services, Directorate for Information Operations and Reports, 1215 Jefferson Davis Highway, Suite 1204, Arlington, VA 22202-4302, and to the Office of Management and Budget, Paperwork Reduction Project (0704-0188), Washington, DC 20503.</small>				
1. AGENCY USE ONLY (Leave blank)		2. REPORT DATE June 1992		3. REPORT TYPE AND DATES COVERED Final, Oct 90 - Sep 91
4. TITLE AND SUBTITLE Theory and Experiment for an Ablating-Capillary Discharge and Application to Electrothermal-Chemical Guns			5. FUNDING NUMBERS PR: 1F2Z9W9XDGS3	
6. AUTHOR(S) John. D. Powell and Alexander E. Zielinski				
7. PERFORMING ORGANIZATION NAME(S) AND ADDRESS(ES)			8. PERFORMING ORGANIZATION REPORT NUMBER	
9. SPONSORING / MONITORING AGENCY NAME(S) AND ADDRESS(ES) U.S. Army Ballistic Research Laboratory ATTN: SLCBR-DD-T Aberdeen Proving Ground, MD 21005-5066			10. SPONSORING / MONITORING AGENCY REPORT NUMBER BRL-TR-3355	
11. SUPPLEMENTARY NOTES				
12a. DISTRIBUTION / AVAILABILITY STATEMENT Approved for public release; distribution is unlimited.			12b. DISTRIBUTION CODE	
13. ABSTRACT (Maximum 200 words) A one-dimensional model is developed for calculating the properties of plasma arcs in ablating, cylindrical capillaries. The objective of the work is to provide information concerning these plasmas which can ultimately be coupled to models of both the working fluid and the power supply in electrothermal guns. Various limiting-case approximations to the model are described. A number of diagnostic measurements are then discussed for eight separate shots in which an arc was discharged into a long, open-ended, brass tube. The capillary for these shots consisted of a polyethylene tube. The measurements included the pulsed current supplied by the power supply, the voltage across the capillary, and the pressure within the capillary measured at a point near the breech or anode end of the tube. All measurements were made as a function of time for the duration of the current pulse. Results from the experiments are then compared with various calculations undertaken with the model. The degree to which the theory and experiment agree is discussed in some detail, and possible reasons for the lack of agreement, where it exists, are pointed out.				
14. SUBJECT TERMS electrothermal guns, plasma discharge, plasma devices, plasma jets			15. NUMBER OF PAGES 67	
			16. PRICE CODE	
17. SECURITY CLASSIFICATION OF REPORT UNCLASSIFIED	18. SECURITY CLASSIFICATION OF THIS PAGE UNCLASSIFIED	19. SECURITY CLASSIFICATION OF ABSTRACT UNCLASSIFIED	20. LIMITATION OF ABSTRACT SAR	

INTENTIONALLY LEFT BLANK.

TABLE OF CONTENTS

	<u>Page</u>
LIST OF FIGURES	v
LIST OF TABLES	vii
ACKNOWLEDGMENT	ix
1. INTRODUCTION	1
2. MODEL AND ASSUMPTIONS	2
3. THEORETICAL FORMALISM	4
3.1 Derivation of Conservation Equations with Ablation	4
3.2 Equations of State and Supplementary Relations	7
3.3 Solution of Governing Equations	12
4. THE STEADY-STATE, ISOTHERMAL MODEL	14
5. EXPERIMENT	16
5.1 Experimental Set-up	17
5.2 Diagnostics	18
5.3 Measured Data	21
5.4 Pressure-Gage Calibration	29
6. CALCULATIONS AND COMPARISON WITH EXPERIMENT	32
6.1 Steady-State Calculations	33
6.2 Time-Dependent Calculations	36
6.3 Calculations Employing Measured Pressure as Input	43
7. CONCLUSIONS AND DISCUSSION	45
8. REFERENCES	49
DISTRIBUTION LIST	51



Accession For	
NTIS GRAM1	<input checked="" type="checkbox"/>
DTIC TAB	<input type="checkbox"/>
Unannounced	<input type="checkbox"/>
Justification	
by	
on (date)	
A-1	
Special	
Dist	
A-1	

INTENTIONALLY LEFT BLANK.

LIST OF FIGURES

<u>Figure</u>	<u>Page</u>
1. Schematic Diagram of Capillary Model.	3
2. Illustration of the Circuit for the 400-kJ Power Supply. Only the first module is shown explicitly.	18
3. Capillary Experiment Connected to the 400-kJ, Pulsed Power Supply.	19
4. Four Measured Module Inductor Currents as a Function of Time for Shot 8.	22
5. Measured Plasma Arc Current as a Function of Time for Shot 8.	23
6. Measured Anode-to-Housing Voltage Drop as a Function of Time for Shot 8.	24
7. Measured Pressure as a Function of Time for Shot 8.	25
8. Reference Pressure and Capillary Pressure as a Function of Time.	30
9. Calibration Factor as a Function of Measured Capillary Pressure. Data are for falling pressure.	31
10. Calibration Factor as a Function of Measured Capillary Pressure. Data are for rising pressure.	31
11. Comparison of Steady-State Pressure Profiles in the Isothermal and General Models for Shot 8.	36
12. Comparison of Steady-State Temperature Profiles in the Isothermal and Gen- eral Models for Shot 8.	37
13. Calculated Pressure Profiles at Several Times for Shot 8.	38
14. Calculated Velocity Profiles at Several Times for Shot 8.	39
15. Calculated Temperature Profiles at Several Times for Shot 8.	39
16. Experimental and Calculated Values of the Conductance as a Function of Current for Shot 8.	41
17. Experimental and Calculated Values of the Pressure as a Function of Current for Shot 8.	41
18. Experimental and Calculated Values of the Conductance as a Function of Current for Shot 4.	42
19. Experimental and Calculated Values of the Pressure as a Function of Current for Shot 4.	42
20. Measured and Theoretical Values of the Conductance for Sonic and Nonsonic Exit-Flow Conditions. The results are for Shot 8.	44
21. Plasma Mach Number at Exit Plane for the Pressure-Match Calculation.	45

INTENTIONALLY LEFT BLANK.

LIST OF TABLES

<u>Table</u>		<u>Page</u>
1.	Degeneracy Factors and Electronic Energy Levels for Hydrogen, Carbon, and Their Ions	10
2.	Summary of Measured Data	27
3.	Peak Data	27
4.	Summary of Energy-Conversion Data	28
5.	Summary of Calibration Constants for the Capillary Gage	32
6.	Calculations with Isothermal, Steady-State Model and Comparison with Experimental Results.	34
7.	Theoretical Results from Time-Dependent Calculations for Shot 8.	40

INTENTIONALLY LEFT BLANK.

Acknowledgment

We wish to thank the following persons: Mr. Henry Burden for much helpful guidance in the experimental aspects of this work, and for his careful review of the final manuscript; Dr. Jad Batteli for many useful discussions concerning the results of the calculations and for constructive criticism of the model; Dr. Donald Ecclesshall for useful discussion of the significance of the time-dependent behavior of the plasma discharge; Ms. Gloria Wren for her support and helpful remarks, particularly concerning the applicability of the work to electrothermal guns; Messrs. H. Kahn and H. Moore for continued support for experimental work in propulsion technology; and Mr. Steven C. Niles for assistance in the laboratory and advice concerning the experimental operations.

INTENTIONALLY LEFT BLANK.

1. INTRODUCTION

In recent work, referred to as PZ1 (Powell and Zielinski 1989), we developed a steady-state model for investigating the properties of plasma discharges in an electrothermal (ET) gun. A number of experimental measurements were also discussed and a comparison of the experimental and theoretical results was undertaken. In this report, we will be interested primarily in extending the calculations to the time-dependent regime. We will also account for certain nonideal effects, neglected in our previous work, but which can be important for plasmas in the temperature and density range characteristic of these discharges. More extensive experimental measurements will also be presented and compared with the calculations. It is, in fact, these additional measurements and their lack of agreement with the steady-state model that have motivated the time-dependent calculations.

The intent of both the theoretical and experimental work described here is to provide some insight into the nature of the capillary discharge. It is hoped that ultimately a model can be developed which can be coupled to interior-ballistic codes, as well as to models for the appropriate power supplies, and provide a complete description of the electrothermal gun. The complexity of the analysis as a whole has been the basic motivation for various groups concentrating on a single aspect of the problem.

During the last decade or so, considerable effort has been expended in the study of problems similar to the capillary discharge. This emphasis has arisen because of the importance of ablation-stabilized arcs for a variety of applications. Probably the most complete experimental work was the early investigations by Ibrahim (1980) who undertook quite an extensive set of diagnostic measurements of various arc properties. A fairly simple theoretical model was also proposed and used to analyze the experimental data. Later, Kovitya and Lowke (1984) undertook a thoroughgoing theoretical treatment of the problem. Their model was one-dimensional and predicted the properties of the discharge under steady-state conditions. Results of the calculations were compared to a very limited extent with the experimental work of Ibrahim (1980), and also of Niemeyer (1978), and reasonably good agreement between theory and experiment was claimed. More recent work, both theoretical and experimental, has been carried out by Ruciti and Niemeyer (1986). With regard to the specific problem of electrothermal-gun capillaries, models of varying complexity have been proposed by Tidman, Thio, Goldstein, and Spicer (1986), by Loeb and Kaplan (1989), by Chrysomallis, Marinos, Ricci, and Cook (1988), by Mohanti, Gilligan, and Bourham (Mohanti and Gilligan 1990; Mohanti, Gilligan, and Bourham 1991), and by various investigators at Sandia National Laboratories (Woodfin 1991). These treatments range from zero dimensional and steady state, to more sophisticated time-dependent, one-dimensional calculations

which are coupled to both the pulse-forming network and to interior-ballistic models of the working fluid.

The model and calculations both here and in our previous work are similar to the one-dimensional treatments above. Our intention has been to develop a capability in BRL for describing the ET capillary in order to provide basic data for modeling the interior ballistics of these devices. Furthermore, we have available models and computer codes that were developed in conjunction with the study of plasma arcs in railguns. These codes solve the basic magnetohydrodynamic conservation equations for the plasma, as well as calculate its conductivity, its ionization state, and approximate pertinent equations of state. This report will basically describe our first efforts at modifying these models and programs to treat the ET-capillary problem, as well as present some preliminary experimental measurements of the plasma properties.

The organization of the report is as follows. In Sec. 2, we describe the model and major assumptions. In Sec. 3, the theoretical formalism necessary for treating the problem is developed. In Sec. 4, we discuss a simple, limiting-case calculation; the simplified model is one which is isothermal and steady state. In Sec. 5, the experimental measurements alluded to above are described in some detail. Section 6 contains results of the calculations and a comparison of theoretical and experimental results. Finally, in Sec. 7, we attempt to discuss rather carefully the limitations of the calculations, likely reasons for the lack of agreement between some aspects of calculations and experiment, and some ways in which both the model and experiments can be improved in future work.

2. MODEL AND ASSUMPTIONS

The basic model that will be employed in the calculations is shown schematically in Fig. 1. A potential difference applied between the anode and cathode, located at $z = 0$ and $z = \ell$ in the figure, produces a current i which is conducted through a plasma arc in the interior of the cylinder shown. The current ohmically heats the plasma to temperatures of several tens of thousands of degrees. Radiation flux \bar{q} from the heated plasma then ablates additional material from the capillary wall. This material replaces the plasma which is shown, via the curved arrows, flowing out the end of the capillary tube located at $z = \ell$. The left end of the tube, located at $z = 0$, is closed. The radius of the capillary, not shown in the figure, is r_b .

In PZ., we undertook calculations with this model in which it was assumed that the plasma could be treated in the steady-state approximation. In the present work we will extend those calculations to the time-dependent regime. In addition, we will include certain

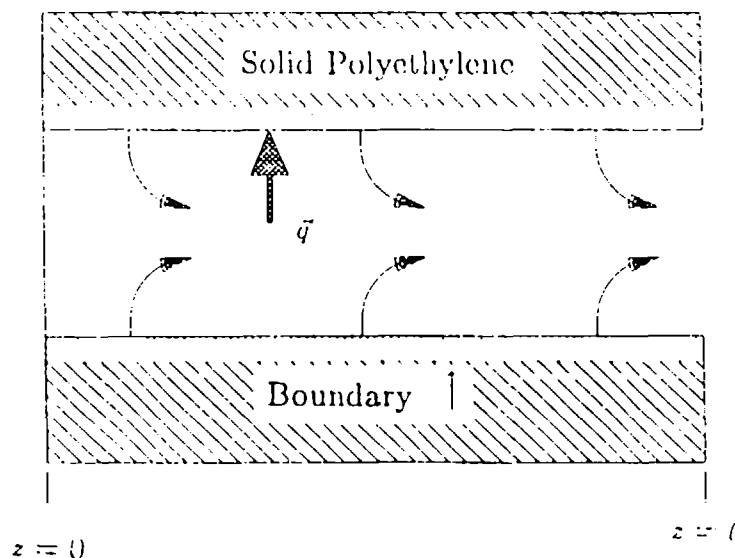


Figure 1. Schematic Diagram of Capillary Model.

nonideal effects which can occur for plasmas in this temperature and density range. These nonideal effects are important whenever the density of the plasma is sufficiently high that, because of nonnegligible Coulomb interactions, the potential energy is not negligible relative to the thermal energy. Nonideal plasmas have received considerable attention in the last few years, and there now exist an enormous number of models (See, e.g., Gunther and Radtke 1984) for calculating the effects of these important interactions.

Nonideal effects can be expected to produce the following consequences. First, and probably most important, is a reduction in the plasma conductivity at a fixed temperature and pressure. Roughly speaking, this reduction occurs because short-range collisions between electrons and ions, which occur infrequently and are negligible in low-density plasmas, cannot be neglected in the nonideal case. To correct the conductivity, we have adapted a heuristic method developed by Zollweg and Liebermann (1987), the principal result of which is to replace the Debye shielding parameter in the usual Spitzer expression (Spitzer 1965) for conductivity by an effective, larger value. The second consequence of nonnegligible Coulomb interactions is that the nominally "free" electrons in the plasma are no longer completely free, but remain weakly bound to the ions. Consequently, there is an effective reduction in the ionization potential associated with each species, since less energy is required to remove an electron to a weakly bound state than to a completely free state. In addition, one can obviously expect a contribution to the internal energy of the plasma from the Coulomb interaction and a resulting change in the pressure as a function of temperature and density.

Since the Coulomb interaction is negative, the pressure is reduced from that which would be obtained in the ideal case. Since the change in both the energy and pressure tend to be very small indeed, at least for cases of interest to us, we have neglected these particular nonideal effects. We do, however, account for the lowering of ionization potential. A similar approximation has been employed for railgun plasma armatures by Rolader and Battch (1989), and we will use the same model for the ionization reduction as they have employed. The model is that developed by Ebeling and Sandig (1973).

Two other minor improvements have been made in the calculations of PZ1. First, we have attempted to improve the computation of the electronic partition functions of carbon and its ions by including additional terms in the series. Second, we have included a calculation of the electronic excitation energy and included this contribution in the internal energy of the plasma. Both of these changes are discussed in greater detail in the ensuing pages, but neither makes a particularly significant change in the results of PZ1.

Other approximations and assumptions that were employed in PZ1 are also used in this calculation: The model is one dimensional so that it is assumed that all flow variables are nearly constant across the cross section of the capillary, except possibly within a small distance of width δ near the walls. This region is designated as the "boundary" and is so labelled in Fig. 1. In all final equations we take the limit as $\delta \rightarrow 0$. It is assumed that the plasma consists of a homogeneous mixture of hydrogen and carbon neutrals and ions, which resulted from dissociated polyethylene, the substance assumed to compose the solid capillary. The carbon is assumed to be at most doubly ionized. We neglect both turbulent and magnetohydrodynamic effects. The latter approximation is reasonable since the magnetic pressures turn out to be small relative to the hydrostatic pressures; the neglect of turbulence is not so easily justified and requires further study.

3. THEORETICAL FORMALISM

3.1 Derivation of Conservation Equations with Ablation. The most straightforward method for obtaining the one-dimensional equations which express conservation of mass, momentum, and energy and which account for ablation is to average the appropriate two-dimensional equations over the cross section of the capillary. We therefore begin the analysis with the standard axisymmetric two-dimensional results in cylindrical coordinates. Let ρ , P , and E be the density, pressure, and specific internal energy of the plasma. Let \vec{v} be velocity which has r component u and z component w . Let J , σ , and \vec{q} be the current density, electrical conductivity, and heat flux. Then, expressed in conservation form, the equations can be written

$$\frac{\partial \rho}{\partial t} + \frac{1}{r} \frac{\partial}{\partial r}(r \rho u) + \frac{\partial}{\partial z}(\rho w) = 0 \quad (1)$$

$$\frac{\partial}{\partial t}(\rho w) + \frac{1}{r} \frac{\partial}{\partial r}(r \rho u w) + \frac{\partial}{\partial z}(\rho w^2) = -\frac{\partial P}{\partial z} \quad (2)$$

and

$$\begin{aligned} \frac{\partial}{\partial t}[\rho(E + v^2/2)] + \frac{1}{r} \frac{\partial}{\partial r}[r \rho u(E + v^2/2)] + \frac{\partial}{\partial z}[\rho w(E + v^2/2)] + \frac{1}{r} \frac{\partial}{\partial r}(r P u) + \frac{\partial}{\partial z}(P w) = \\ \frac{J^2}{\sigma} - \frac{1}{r} \frac{\partial}{\partial r}(r q_r) - \frac{\partial q_z}{\partial z}. \end{aligned} \quad (3)$$

We now assume that all the plasma variables are nearly constant across the arc cross section except very near the boundary. We then multiply through each of the equations above by $2\pi r dr$ and integrate from $r = 0$ to $r = r_b - \delta$, i. e., up to the inside edge of the boundary layer. The spatial average of any variable F is defined as

$$\bar{F} = \frac{2\pi}{A} \int_0^{r_b} r F(r, z) dr \quad (4)$$

where A is the cross sectional area given by $A = \pi r_b^2$. In obtaining the above result we have taken δ to be small relative to r_b . We furthermore assume that since the variables are nearly constant that the average of all products can be replaced by the product of averages. The above integrations then yield

$$\frac{\partial \bar{\rho}}{\partial t} + \frac{\partial}{\partial z}(\bar{\rho} \bar{w}) = -\frac{2}{r_b} \rho_b u_b = \dot{\rho}_a \quad (5)$$

$$\frac{\partial}{\partial t}(\bar{\rho} \bar{w}) + \frac{\partial}{\partial z}(\bar{\rho} \bar{w}^2) + \frac{2}{r_b}(\rho_b u_b w_b) = -\frac{\partial \bar{P}}{\partial z} \quad (6)$$

and

$$\begin{aligned} \frac{\partial}{\partial t}[\bar{\rho}(\bar{E} + \bar{v}^2/2)] + \frac{\partial}{\partial z}[\bar{\rho} \bar{w}(\bar{E} + \bar{v}^2/2)] + \frac{\partial}{\partial z}(\bar{P} \bar{w}) = \bar{J}^2/\bar{\sigma} - \frac{\partial \bar{Q}_z}{\partial z} - \frac{2}{r_b} \bar{P}_b u_b - \\ \frac{2}{r_b} \rho_b u_b (\bar{E}_b + \bar{v}_b^2/2) - \frac{2}{r_b} q_{rb}. \end{aligned} \quad (7)$$

Here the subscript b denotes values of the variable in question at the point $r = r_b - \delta$. In obtaining Eq. (7), we have assumed that $\bar{v}^2 \simeq \bar{w}^2$ and, since A changes only by a small amount in any calculation of interest to us, we have also taken $\partial A/\partial t$ and $\partial A/\partial z$ to be zero. We will henceforth assume that $w_b = 0$ in accordance with previous assumptions (Powell and Zielinski 1989) that the ablated products enter with no velocity and neglect the last term on the left-hand side of Eq. (6).

In order to obtain the rate of ablation, it is necessary to observe that Eqs. (1) and (3), which express conservation of mass and energy, hold not only in the plasma but in the solid polyethylene as well provided we take $\bar{v} = 0$. As a result, the equations imply certain boundary conditions that must hold at the interface between the plasma and the solid. These conditions can be obtained by integrating each of the equations across the boundary of thickness δ and then taking the limit as $\delta \rightarrow 0$. We finally observe that the integral of each partial time derivative $\frac{\partial F}{\partial t}$ produces, except for terms which vanish with δ , the result $-\dot{r}_b < F >$. Here \dot{r}_b denotes the velocity with which the boundary moves and the brackets (in this section only) denote the change in the quantity in question as the boundary is crossed. Carrying out the two integrations then and solving the results for u_b and \dot{r}_b , we obtain

$$u_b = -\frac{\Delta q}{P_b + \rho_b E_b} \quad (8)$$

and

$$\dot{r}_b = \frac{\rho_s \Delta q}{\rho_s (P_b + \rho_b E_b)}. \quad (9)$$

In these two equations ρ_s denotes the density of solid polyethylene, and $\Delta q = q_{rb} - q_{rs}$ denotes the difference in the flux emitted by the gas at the boundary and that transmitted all the way into the solid or, in other words, the flux absorbed by the boundary. In deriving these equations we have assumed that $\rho_s \gg \rho_b$, $E_s \ll E_b$, and $u_b^2 \ll E_b$. Equation (8) can evidently be used to obtain the ablation rate, whereas Eq. (9) yields the rate at which the solid surface recedes.

Equations (8) and (9) can now be used in Eqs. (5)-(7). We find after expanding out the derivatives and simplifying the equations considerably that the results can be written

$$\frac{\partial \rho}{\partial t} + \rho \frac{\partial w}{\partial z} + w \frac{\partial \rho}{\partial z} = \dot{\rho}_a \quad (10)$$

$$\rho \frac{\partial w}{\partial t} + \rho w \frac{\partial w}{\partial z} + w \dot{\rho}_a = - \frac{\partial P}{\partial z} \quad (11)$$

and

$$\rho \frac{\partial E}{\partial t} + \rho w \frac{\partial E}{\partial z} + P \frac{\partial w}{\partial z} + \dot{\rho}_a (E - w^2/2) = \frac{J^2}{\sigma} - \frac{2}{r_b} q_{rs} - \frac{\partial q_z}{\partial z}. \quad (12)$$

with the ablation rate $\dot{\rho}_a$ given by

$$\dot{\rho}_a = \frac{2\rho_b \Delta q}{r_b(P_b + \rho_b E_b)}. \quad (13)$$

The overbars, denoting average values, have for simplicity been omitted in these equations and will be omitted in the remainder of the report. It is to be understood that averaged values are implied unless stated otherwise. Equations similar to those above have been derived, for example, by Tidman, Thio, Goldstein, and Spicer (1986).

The ablation-dependent terms in the above equations can be interpreted as follows. The term $\dot{\rho}_a$ in Eq. (10) represents the rate at which the plasma density increases because of ablation. The term $w\dot{\rho}_a$ in Eq. (11) represents a drag force on the gas because the ablated products enter with no velocity. Finally, in Eq. (12), the term $\dot{\rho}_a E$ accounts for energy expended by the plasma to bring about the ablation process, whereas the term $\dot{\rho}_a w^2/2$ corresponds to a dissipative effect resulting again from the ablation products entering the mainstream of the arc with no velocity. The first of the last two terms results in a decrease in internal energy, while the second results in an increase.

3.2 Equations of State and Supplementary Relations. As is well known, the conservation equations presented in the previous section are not sufficient to determine uniquely the various fluid parameters. Additional relations required include expressions for the heat flux \tilde{q} and conductivity σ , as well as equations of state which relate P and E to the density ρ and temperature T . Much of these data have been tabulated for polyethylene in, for example, the SESAME tables (Holian 1984). Nevertheless, we will formulate the appropriate relations in their entirety and carry out the calculations within the computer code. The purpose for undertaking the calculations rather than relying on tabulated or curve-fitted values is our interest in developing a mechanism whereby plasma constituents may be changed easily, even for mixtures whose properties have not been previously documented.

In all the calculations to be discussed, we will neglect both the longitudinal heat flux q_z as well as the flux conducted into the solid polyethylene, q_{rs} . The first effect was deemed

negligible because the length of our capillary tubes is generally large compared to their radius. Moreover, earlier calculations which we have performed including this effect suggested only minor differences with cases in which it was neglected. The second effect is assumed to be fairly insignificant because of the low thermal conductivity of polyethylene. The energy flux radiated out the sides of the capillary will be assumed to obey the standard blackbody-radiation result. Consequently, we will neglect the last two terms on the right-hand side of Eq. (12), and take Δq in Eqs. (8) and (9) to be given by

$$\Delta q = q_{rb} = \sigma_S T_b^4, \quad (14)$$

where σ_S is Stefan's constant.

To determine the pressure equation of state, we assume the law of partial pressures and write

$$P = n_C(1 + x_{1C} + 2x_{2C})kT + n_H(1 + x_{1H})kT, \quad (15)$$

where k is Boltzmann's constant, where n_C and n_H denote the number densities of heavy particles for carbon and hydrogen, respectively, and where $x_{j\alpha}$ is used to denote the ratio of "jth" ions to heavy particles for species α . We assume that the carbon atoms are ionized at most doubly, an assumption which will prove reasonable for the temperature and density ranges of interest. It is sometimes convenient to express Eq. (15) in terms of the mass density and to use the rather obvious relation

$$n_C = \frac{\rho}{m_{0C} + r_0 m_{0H}}, \quad (16)$$

where m_{0C} and m_{0H} are the masses of the carbon and hydrogen atoms, respectively, and r_0 is the ratio of hydrogen to carbon heavy particles. For the assumed homogeneous mixture of polyethylene, $r_0 = 2$.

The ion concentrations which appear in Eq. (15) can be determined by solving the Saha equations (see, e. g., Zeldovich and Raizer 1966). In rather simplified notation these governing equations can be written

$$x_{2\alpha} = K_{2\alpha} x_{1\alpha} = \frac{K_{1\alpha} K_{2\alpha}}{1 + K_{1\alpha} + K_{1\alpha} K_{2\alpha}}. \quad (17)$$

The functions $K_{j\alpha}$ are given by

$$K_{j\alpha} = \frac{2}{n_e} \frac{Z_{j\alpha}}{Z_{\alpha,j-1}} \left(\frac{2\pi m_e kT}{h^2} \right)^{3/2} \exp[-(I_{j\alpha} - \Delta I_{j\alpha})/kT], \quad (18)$$

where m_e is the electron mass, h is Planck's constant, $I_{j\alpha}$ denotes the j th ionization potential for specie α , and $\Delta I_{j\alpha}$ denotes the reduction in the ionization potential because of the nonideal effects discussed earlier. As pointed out, we use the model proposed by Ebeling and Sandig (1973) to compute the reduced potentials. The reduction can then be written

$$\Delta I_{j\alpha} = \frac{j e^2}{4\pi\epsilon_0(\lambda_D + \bar{\Lambda}/8)}. \quad (19)$$

In this expression ϵ_0 is the permittivity of free space, e is the electronic charge, and $\bar{\Lambda}$ is the deBroglie wavelength given by

$$\bar{\Lambda} = \frac{h}{(2\pi m_e kT)^{1/2}}. \quad (20)$$

The parameter λ_D is the standard Debye length, taken here to account for both electron and positive-ion shielding, and can be written

$$\lambda_D = \left[\frac{\epsilon_0 kT}{n_e e^2 (1 + Z)} \right]^{1/2} \quad (21)$$

where n_e is the electron density given by

$$n_e = n_{1H} + n_{1C} + 2n_{2C}, \quad (22)$$

and Z represents the effective charge on an ion, namely,

$$Z = \frac{n_C x_{1C} + 4n_C x_{2C} + n_H x_{1H}}{n_C x_{1C} + 2n_C x_{2C} + n_H x_{1H}}. \quad (23)$$

The electronic partition functions $Z_{j\alpha}$ which appear in Eq. (18) can be written (Zeldovich and Raizer 1966)

$$Z_{j\alpha} = \sum_i g_{j\alpha i} \exp(-U_{j\alpha i}/kT), \quad (24)$$

where $U_{j\alpha i}$ is the energy level of the i th electronic state of the j th ion, and $g_{j\alpha i}$ is the appropriate degeneracy factor for this level. These energy-level data have been compiled

Table 1. Degeneracy Factors and Electronic Energy Levels for Hydrogen, Carbon, and Their Ions

	Carbon						Hydrogen	
	$I_{1C}=11.26 \text{ ev}$ $j = 0$		$I_{2C}= 24.38 \text{ ev}$ $j = 1$		$I_{3C}=47.86 \text{ ev}$ $j = 2$		$I_{1H}=13.60 \text{ ev}$ $j = 0$	
i	g_{0Ci}	$U_{0Ci}(\text{ev})$	g_{1Ci}	$U_{1Ci}(\text{ev})$	g_{2Ci}	$U_{2Ci}(\text{ev})$	g_{0Hi}	$U_{0Hi}(\text{ev})$
1	1	0.0	2	0.0	1	0.0	2	0.0
2	3	0.0020	4	0.0079	9	6.50		
3	5	0.0054	12	5.35				
4	5	1.27						
5	1	2.69						
6	5	4.19						
7	9	7.50						
8	3	7.70						
9	15	7.96						
10	3	8.56						
11	15	8.66						
12	3	8.79						
13	9	8.87						

elsewhere (Moore 1952). The summation in Eq. (24) should actually be extended over all levels having energy lower than the reduced ionization potential. For simplicity, however, we have extended the sum only over levels whose energy was less than about 9 ev. Our calculations will indicate temperatures within the arc of at most about 3 ev, so that the exponential factors in the omitted terms are at worst about 5% of those in the leading terms. Approximations of this type are fairly common and have been discussed elsewhere (Cambel 1963). The actual levels and degeneracy factors used in the calculations have been indicated in Table 1. It should be noted that in some cases several levels of comparable energy have been grouped together.

In calculating the specific internal energy of the plasma there is a certain arbitrariness in what one defines as the zero level. In calculations which include ablation, however, it is necessary to account for the energy required to vaporize, dissociate, and ionize the solid polyethylene, as well as to heat the resulting products up to the temperature of the plasma

core. One should also account for the electronic excitation energy in both the neutrals and the ions, though this contribution is frequently negligible. If we take the zero energy level to correspond to an unionized gas at zero degrees, the appropriate expression can be written

$$E = \frac{1}{\rho} \left[\frac{3}{2} kT n_C (1 + x_{1C} + 2x_{2C}) + \frac{3}{2} kT n_H (1 + x_{1H}) + (I_{1C} - \Delta I_{1C}) n_C x_{1C} + \right. \quad (25)$$

$$(I_{1H} - \Delta I_{1H}) n_H x_{1H} + (I_{1C} + I_{2C} - \Delta I_{1C} - \Delta I_{2C}) n_C x_{2C} + \rho E_v + \rho E_D +$$

$$n_C (1 - x_{1C} - x_{2C}) W_{0C} + n_C x_{1C} W_{1C} + n_C x_{2C} W_{2C} + n_H (1 - x_{1H}) W_{0H} \}. \quad (25)$$

The quantities E_v and E_D are the specific vaporization and dissociation energies of polyethylene, taken to be given by 2 kJ/g and 80 kJ/g, respectively; the quantities $W_{j\alpha}$ are the electronic excitation energies and can be obtained from the various partition functions via the relation

$$W_{j\alpha} = -kT^2 \frac{\partial Z_{j\alpha}}{\partial T}. \quad (26)$$

This representation of the internal energy neglects the difference in the specific heats of the solid and gas, but the difference is negligible at the high temperatures under consideration.

Finally, we must obtain an expression for the electrical conductivity σ . We account for electron collisions with both ions and neutrals and have from standard relations

$$\sigma = \frac{n_e e^2}{m_e (\nu_{en} + \nu_{ei})}, \quad (27)$$

where ν_{en} and ν_{ei} represent the collision frequencies of electrons with neutrals and ions, respectively. If we assume that the frequencies representing electron-neutral collisions can be added, the appropriate overall frequency can be written in terms the scattering cross sections of neutral hydrogen and carbon as

$$\nu_{en} = v_e [(1 - x_{1C} - x_{2C}) n_C A_C + (1 - x_{1H}) n_H A_H], \quad (28)$$

where v_e denotes the mean electron velocity, namely,

$$v_e = \left(\frac{8kT}{\pi m_e} \right)^{1/2}, \quad (29)$$

and where A_C and A_H denote cross sections of carbon and hydrogen, respectively. In all calculations, we have used the values (Loeb and Kaplan 1989) $A_C = 30\pi a_0^2$ and $A_H = 17\pi a_0^2$ where a_0 is the Bohr radius, approximately equal to 5.29×10^{-11} m.

For the collision frequency with ions, we have used the Spitzer formula but modified in the manner discussed earlier in order to account for nonideal effects. In particular, the well-known "log Λ " term in the usual Spitzer expression is replaced by (Zollweg and Liebermann 1987)

$$\log \Lambda \rightarrow \log (1 + 1.4\Lambda_m^2)^{1/2}, \quad (30)$$

where Λ_m is given by

$$\Lambda_m = \frac{12\pi\epsilon_0 kT}{Ze^2} \left[\frac{\epsilon_0 kT}{n_e e^2} + \left(\frac{3}{4\pi n_+} \right)^{2/3} \right]^{1/2} \quad (31)$$

and n_+ denotes the density of positive ions in the plasma. In terms of other quantities calculated, we have

$$n_+ = n_C(x_{1C} + x_{2C}) + n_H x_{1H}. \quad (32)$$

As a result of these substitutions, the Spitzer collision frequency becomes

$$\nu_{ei} = \frac{38Zn_e e^2 \log(1 + 1.4\Lambda_m^2)^{1/2}}{\gamma_e m_e T^{3/2}} \quad (33)$$

where γ_e is a fairly weak function of Z approximately equal to 0.58 at $Z = 1$ and 0.68 at $Z = 2$. At points between the extremes, the parameter can be approximated by a linear function with little error. It is possible to show that Eq. (33) reduces to the usual Spitzer result for sufficiently low densities and sufficiently high temperatures.

3.3 Solution of Governing Equations. The formalism developed in the previous two subsections is sufficient to determine the basic flow properties of the plasma in the capillary arc. In particular, if we regard ρ , w , E , $\dot{\rho}_a$, T , and P as the principal variables, then Eqs. (10), (11), (12), (13), (25), and (15) are sufficient to determine these unknowns. The differential equations must be solved subject to some set of initial and boundary conditions. One obvious condition is that

$$w(z = 0) = 0. \quad (34)$$

since the breech end of the capillary is closed. There is an additional condition, which is usually taken to be the flow rate or perhaps the pressure, that must be applied at the capillary exit. The additional condition arises because the gas in the capillary is in general coupled to conditions outside the capillary, and the gas beyond the exit point is not considered in the calculation. Various arguments have been made to suggest that the flow is choked at exit provided the plasma is exhausted into gas contained in a sufficiently large volume and we will generally apply some boundary condition that approximates this situation. If longitudinal heat conduction is accounted for, additional boundary conditions must be specified concerning either the temperature or heat flux at both the breech and exit ends, but generally heat transport in the axial direction has been neglected in the calculations. The initial conditions on the various variables will be discussed in Sec. 6 when specific calculations are undertaken. Finally, it necessary to assume values for the flow variables just inside the capillary-wall boundary, i. e., T_b , ρ_b , P_b , and E_b in Eqs. (13) and (14). Unless otherwise stated we will assume that these values are approximately given by their values in the mainstream of the arc. Such an assumption is consistent with the one-dimensional nature of the model.

In order to solve the differential equations represented by Eqs. (10)-(12), we represented the derivatives in the usual finite-difference approximation. The resulting nonlinear algebraic equations were solved by a completely implicit, modified Newton-Raphson method (Pizer 1975). Various values of the grid spacing and time step were employed, but generally we found that $\Delta z = 0.02\ell$ and $\Delta t = 5 \times 10^{-8}s$ provided sufficient accuracy. An artificial viscosity was included in the time-dependent calculations to extend shock fronts over several grid spacings if negative velocity gradients appear in the calculations. The specific expression used was that of von Neumann and Richtmyer (1950), viz.,

$$\tilde{Q} = -\rho \Delta z^2 b^2 \left(\frac{\partial w}{\partial z} \right)^2, \quad \text{for } \frac{\partial w}{\partial z} < 0 \quad (35)$$

and

$$\tilde{Q} = 0, \quad \text{for } \frac{\partial w}{\partial z} \geq 0.$$

In this expression, b is an arbitrary number of order unity and we have used the value $b = 1.5$. The artificial viscosity is included in the numerical calculations by simply replacing P by $P - \tilde{Q}$ in Eqs. (11) and (12).

4. THE STEADY-STATE, ISOTHERMAL MODEL

It will become evident when we undertake some of the numerical solutions of the general time-dependent equations, that the temperature remains fairly nearly constant across the length of the arc. Furthermore, in most cases, the current changes on a time scale that is slow compared to the rate at which various hydrodynamic processes occur within the plasma. Under such conditions it seems reasonable to approximate the solution of the equations in Sec. 3 with an isothermal, steady-state solution. Careful examination of the equations reveals that a consistent isothermal solution can be found provided the following additional assumptions and approximations are made: (i) in addition to the temperature, the ion concentrations x_{1C} , x_{2C} , and x_{1H} , as well as the conductivity σ , are also position independent; and (ii) the kinetic energy of the plasma can be neglected relative to its internal energy. These assumptions will be shown to be reasonable when the more general calculations are undertaken. The first is acceptable because both the ionization state of the plasma as well as its conductivity are sensitive functions of temperature, but only weak functions of pressure. The second assumption can be shown to hold reasonably well at the high temperatures where there exist many contributions to the internal energy. It can furthermore be shown from the governing equations that, when these two assumptions hold, both $\dot{\rho}_a$ and E are also constant in space.

If we now make these approximations, write the governing differential equations in conservation form, and integrate from zero to z , we obtain the purely algebraic results

$$\rho w = \dot{\rho}_a z \quad (36)$$

$$\rho w^2 + P = P_0 \quad (37)$$

and

$$\rho w E + P w = J^2 z / \sigma. \quad (38)$$

In obtaining these equations, we have used the boundary condition on w represented by Eq. (34) and denoted by P_0 the pressure at the breech end of the capillary. The determination of P_0 must come from the additional boundary condition alluded to in Sec. 3.3 referring to, say, the velocity of the gas at the capillary exit.

If we now substitute Eqs. (36), (13), and (14) into Eq. (38), we can solve formally for the temperature T to produce

$$T = \left(\frac{J^2 r_L}{2\sigma\sigma_s} \right)^{1/4} \quad (39)$$

The above equation expresses that under the stated assumptions the energy dissipated via Joule heating is equivalent to that radiated out the capillary walls, with the kinetic energy being negligible.

We now observe that the pressure equation of state can, according to Eqs. (15) and (16), be written

$$P = C_{s0}^2 \rho, \quad (40)$$

where C_{s0} represents the ion acoustic speed in the plasma under the assumed isothermal conditions and is given explicitly by

$$C_{s0} = \left[\frac{(1 + x_{1C} + 2x_{2C})kT + 2(1 + x_{1H})kT}{m_{0C} + 2m_{0H}} \right]^{1/2}. \quad (41)$$

It may be observed that for the approximations discussed, C_{s0} is also independent of position in the capillary. Substituting this relationship for P into Eq. (37) and solving (36) and (37) for w and ρ produce the explicit relationships

$$\rho = \frac{P_0}{2C_{s0}^2} \left[1 + (1 - 4\dot{\rho}_a^2 C_{s0}^2 z^2 / P_0^2)^{1/2} \right] \quad (42)$$

and

$$w = \frac{2\dot{\rho}_a C_{s0}^2 z}{P_0} \left[1 + (1 - 4\dot{\rho}_a^2 C_{s0}^2 z^2 / P_0^2)^{1/2} \right]^{-1}. \quad (43)$$

Similar expressions for w and ρ have been obtained, for example, by Tidman, Thio, Goldstein, and Spicer (1986). It is evident from the results that a steady solution exists only for

$$P_0 \geq 2\dot{\rho}_a C_{s0}. \quad (44)$$

When the equality holds, the velocity at exit is a maximum and given by the isothermal sound speed C_{s0} .

Even with the preceding simplifications, a completely analytic solution to the governing equations is still not possible since the conductivity and ion concentrations are very complicated functions of the temperature T . Since these quantities are spatially constant, however, the solution to the appropriate equations can be found very easily by iteration and the iteration need not be carried out at every grid point in the domain. More specifically, we solve Eqs. (17), (27), and (39) for x_{1C} , x_{2C} , x_{1H} , σ , and T via iterative techniques; position-dependent variables such as ρ and w , for example, then follow directly from Eqs. (42) and (43) without any additional numerical solutions. In the expressions for σ and the ionization factors, it is necessary of course to express position-dependent quantities such the electron density n_e in Eqs. (18) and (21) by the appropriate value averaged over the length of the arc. This replacement is necessary in order to accord with the assumption that the ionization factors and conductivity do not depend on position. Further study of the equations reveals that all position-dependent quantities in the relevant equations can be expressed as a function of the density ρ and the ionization factors themselves. For example, one can easily show that n_e can be expressed as

$$n_e = \frac{x_{1C} + 2x_{2C} + 2x_{1H}}{m_{0C} + 2m_{0H}} \rho. \quad (45)$$

An expression for $\langle \rho \rangle$,* in turn, follows by integrating Eq. (42) from zero to ℓ and produces the result

$$\langle \rho \rangle = \frac{1}{\ell} \int_0^\ell \rho dz = \frac{P_0}{2C_{s0}^2} \left\{ 1 + \frac{1}{2N} [(N^2 - 1)^{1/2} + N^2 \sin^{-1} 1/N] \right\}, \quad (46)$$

where $N = P_0 / (2\ell \rho_a C_{s0})$.

5. EXPERIMENT

In this section we describe the elements comprising the capillary assembly and the specific measurements made on the plasma discharge. These measurements include the plasma discharge current, the voltage drop across the capillary discharge, and the pressure in the capillary, all as functions of time during each of eight separate shots. Particular emphasis in the discussion will be given to the unique implementation of the pressure transducer.

*The brackets here and in the remainder of the report denote an average over the capillary length.

5.1 Experimental Set-up. The capillary discharge chamber consisted of a 12.7-*mm* outer diameter, 142.8-*mm* long, polyethylene rod, press-fitted into a 27-*mm* outer diameter stainless-steel tube. A 6.35-*mm* diameter, 95-*mm* long, maraging steel rod, coated with a room-temperature vulcanizing adhesive (RTV) and press-fitted into the breech of the capillary, served as the anode electrode. The end of the electrode rod extending from the capillary was threaded to the positive bus from the power supply. The cathode end of the capillary was joined to a 0.254-*m* long brass barrel with a galvanized pipe coupling. The joint was sealed by wrapping teflon tape on the pipe threads and compressing an O-ring in the interface. The capillary and the coupling were compressed between the two 0.05 *m* \times 0.1 *m* \times 0.26 *m* halves of an aluminum housing. The housing was bolted to the ground plate on the power supply and served as the high-current return. The initial diameter of the capillary was 6.35 *mm*. After each firing the diameter of the polyethylene tube was increased with the next larger reamer size. This procedure provided for a new capillary diameter for each shot, but saved valuable time in remachining new capillary parts. The length of the ablating discharge channel was kept constant at 60.9 *mm*.

The pulsed power supply used to perform the experiments consisted of four, 100-*kJ* modules (Zielinski 1989a, 1989b). Each 2000 μF module used a nominal 16 μH pulse-shaping inductor and, for near-zero loads, provided for a current pulse with a 300 μs rise time and a transfer admittance of 11 *kA/kV*. Each module had the flexibility to be charged to different initial voltages as well as to be triggered independently in time. Ignitrons (NL-2888A) were used as closing switches for each module and diodes (12-RA204420's) were included across each module to prevent voltage reversal on the capacitor bank. All module inductors were connected to the positive bus which served to deliver power to the load. For these shots the power supply was configured such that a sinusoidal-type current pulse was produced having a peak current sufficient to yield plasma core temperatures greater than 2 *ev*. The pulse width so greatly exceeded the duration of the time-dependent plasma behavior, that the latter was expected to be negligible. Typically, the initial capacitor voltages were such that the first module, which initiated the plasma, was charged to 1 *kV*, and Modules 2 - 4 were each charged to a progressively higher value of voltage (2 - 5 *kV*). A 100 μs time delay was used between module triggers. A simple illustration of the circuit is shown in Fig. 2.

A 38-gage aluminum wire (\sim 0.114-*mm* diameter), placed along the axial length of the capillary, was used to initiate the plasma discharge. The breech end of the wire was secured between the anode rod and the capillary wall, and the muzzle end between the capillary and the brass barrel. The D.C. resistance was measured between the breech and the aluminum-housing, and was verified to be less than 1 Ω before each shot to ensure a reliable arc initiation. An insulated block-and-screw arrangement was secured behind the anode connec-

tion to prevent loss of capillary pressure and voltage breakdown. As the screw was tightened, an axial force was applied to help seal the anode in the capillary. A picture of the assembled capillary, mounted in the aluminum housing and connected to the pulsed power supply, is shown in Fig. 3.

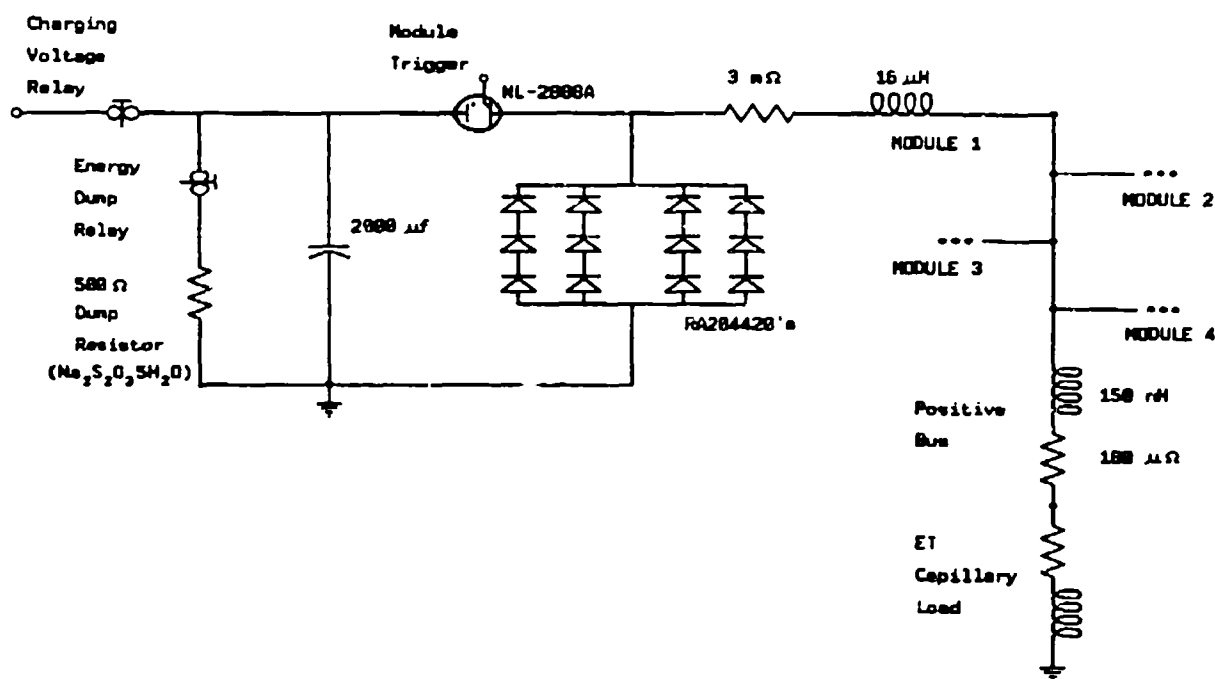


Figure 2. Illustration of the Circuit for the 400-kJ Power Supply. Only the first module is shown explicitly.

5.2 Diagnostics. All of the experimental electrical data were taken using three Nicolet 4094C Digital Oscilloscopes. Most of the data were recorded at a rate of $1.0 \mu\text{s}/\text{point}$ using 12-bit amplifiers (1 MegaSample/s, amplifier model number 4562). The pulsed-power supply incorporated a single-point grounding scheme with the signal cables laid in close proximity to the return ground braid of the oscilloscope. This positioning helped to avoid any induced loop currents in the data-signal lines. The ground braid from the single-point, earth ground was attached to the chassis of each oscilloscope in the control room, and the A.C. conduit ground for each oscilloscope was disconnected. At the oscilloscope, each data line and each A.C. power cord was looped several times through a separate ferrite core. The data were stored on $5\frac{1}{4}$ -inch floppy disks and later transferred to the large computer for analysis.

The pressure transducer used in these experiments was a Kistler gage, model 607C. It has a range up to 689.4 MPa and a sensitivity constant of $-0.147 \text{ pC}/\text{psi}$. A radial, flat-bottomed hole was drilled through the stainless steel tube into the polyethylene wall. A

wall thickness of 1.8 mm (for a 6.35 mm capillary diameter) was left between the gage head and the capillary wall. As the firings progressed, the capillary diameter was enlarged and consequently the wall thickness was reduced. A stainless steel mounting block was also added to the outside of the stainless tube to provide extra support for the mounting threads of the gage. The gage was located 17 mm from the steel anode. An access hole was drilled through the aluminum housing with adequate clearance for insulation around the gage, the RG-174 miniature coaxial cable, and the BNC connector.

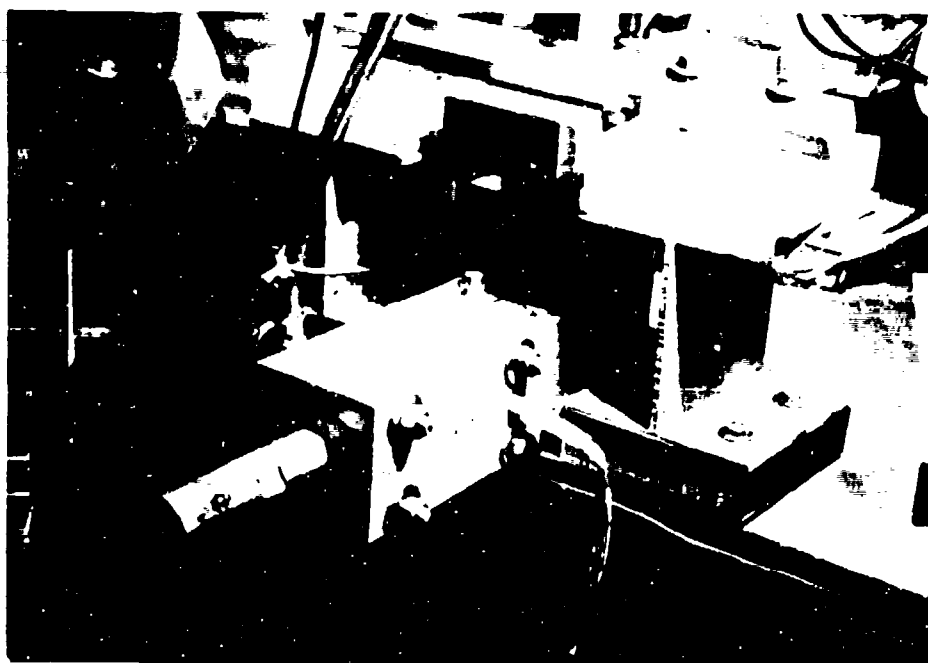


Figure 3. Capillary Experiment Connected to the 400-*kJ*, Pulsed-Power Supply.

Before each test the gage was lightly coated with vacuum grease, inserted in the radial hole, and tightened while the capillary was in a vacuum chamber. This procedure reduced the amount of air trapped between the gage head and polyethylene wall. Typically, a vacuum of a few Pascals ($50 \mu Hg$) was attained in the chamber via use of a roughing pump.

During the course of this work consideration was given to the acquisition of the pressure-transducer signal voltage. Model 607C is a high-impedance, ballistic transducer with a rise time of $1.5 \mu s$ and is well suited for dynamic events. It produces an output of electrical charge proportional to its quartz-crystal displacement. Consequently, a charge amplifier is needed to convert the electrical charge into a voltage signal proportional to the applied pressure. In these experiments a Kistler Dual Mode Amplifier (Model 5004) was used with a short-time-constant setting (i. e., maximum pressure pulse duration of hundreds of milliseconds).

Additionally, the output of this type of amplifier (± 10 V full scale) is current limited and may not preserve the high-frequency content of the transducer signal, particularly when used to drive long coaxial data lines. For this reason full-scale output was kept around 4 V.

The large, rapidly time-varying electric and magnetic fields near the experiment seemed to dictate the use of a fiber-optic data line to obtain consistent, noise-free pressure signals. An amplitude-modulated (AM) transceiver/receiver pair (Manage Incorporated, model numbers FOL-100, PC/Rx, and FOL-100, PC5/Tx) was employed initially. However, the gain of the AM pair was found to be both time and amplitude dependent. Because of the uncertainties in calibration a simple, double-shielded coaxial data line from the experiment to the oscilloscope was tried. Subsequently, the double-shielded technique was employed throughout the remainder of the experiment.

The miniature coaxial cable from the pressure transducer was roughly 1 m long, and located inside a section of ground braid (second shield) which was connected at the stainless-steel capillary tube (essentially at ground potential). The other end of the ground braid was attached to a steel box which contained, but was insulated from, the charge amplifier. Signal noise could easily be introduced into the data-line shields simply by allowing the metal box or outer braid to come into direct contact with the concrete floor. Therefore, the metal box was insulated from the floor with a sheet of wood and mylar. Before the signal line from the pressure gage was connected to the charge amplifier, the cable was wound several times through a large ferrite core. This procedure impeded any ground currents which might be induced in the cable shield. The chassis of the charge amplifier was isolated from A.C. conduit ground by disconnecting the third prong on the power plug and by winding the cord several times through a separate ferrite core. Because the A.C. ground was lifted, there existed approximately 50 V A.C. between the second outer braid and ground. Before the miniature coaxial cable could be connected to the pressure transducer, the outer braid and experiment ground were temporarily connected. In this way any potentially harmful gage current was discharged to ground. Once the signal line was connected, the temporary jumper could be removed and a more substantial ground connection could be made. The aluminum housing was connected to the single-point earth ground located at the experiment. The output coaxial cable from the charge amplifier was double shielded and connected at the metal box and at the oscilloscope input BNC connector. Careful attention was placed on ensuring that the outer ground shield was well insulated along the way to the oscilloscope. Before each firing, a known input voltage was applied to the charge-amplifier calibration input. This procedure was followed to check the charge-amplifier calibration as well as to verify the amplifier-to-oscilloscope signal path.

Additional electrical diagnostics included measurements of the load voltage and the time

rates of change of the plasma and individual module-inductor currents. The voltage was measured between the anode connection block and the aluminum housing by using a Pearson current transformer and resistor string. The time rate of change of the currents was measured with Rogowski coils placed around the positive bus of the pulsed-power supply and each individual inductor lead. These techniques, used previously in railgun experiments, are described elsewhere (Zielinski and Powell 1990).

The plasma discharge current typically rose to peak in about 450 μ s. Monitoring each of four, separate, rapidly-varying current pulses, using Rogowski coils, provided a valuable diagnostic since recorded di/dt signals may contain information on functional anomalies that an integrated waveform would mask. The di/dt signals were recorded directly from the Rogowski coils and the integrations to obtain current performed numerically using a five-point smoothing algorithm. The Rogowski coils used for these experiments had rise times of less than 3 μ s. The error between the sum of the four measured inductor module currents and the measured total arc current for all the shots was typically less than 5%.

5.3 Measured Data. There were eight firings performed in this series of experiments. Current and voltage data were obtained on all firings; five firings produced valid pressure data. The pressure data obtained on the remaining firings were not useful. Solder, used to fill unused fiber-optic velocity measurement holes in the brass barrel, blew out owing to capillary pressure.

Physical measurements in these experiments included the capillary diameter before and after five of the firings and limited video-tape footage during the firings. The changes in dimensions of the capillary were used to estimate the ablated mass and the recession rate of the capillary wall. The video data revealed the large amounts of light and gas being expelled from the brass barrel many frames after the depletion of the capacitive stored energy. Although only qualitative, these data provided insight into additional energy-conversion mechanisms which occur on a time scale greater than the width of the current pulse.

The data sets from each firing exhibited similar features and therefore only one firing, Shot 8, will be discussed in detail. Summaries of measured data from the remaining shots are presented in Tables 2 and 3 and will be given more cursory discussion later.

The arc current, $i(t)$, was comprised of current supplied by the four independently triggered capacitor-bank modules. For Shot 8, the initial charge voltages were 2.0, 3.5, 4.5, and 5.0 kV, on Banks 1-4, respectively. Between each trigger pulse were 100 μ s time delays. The inductor currents of each module are shown in Fig. 4 as a function of time. The first two current pulses rise to their peak in roughly 200 μ s. The rise time for the current of

the remaining modules approaches the short-circuit value ($300 \mu s$), owing to the lowered resistance of the arc at the higher current. The currents presented in the figure are bipolar even though there are diodes across each module to prevent voltage reversal on the capacitor bank. The interaction between the current-dependent load voltage and the module currents causes the capacitor voltage to oscillate about a value above zero potential. Furthermore, on this shot it appeared that the first module had been recharged to a higher voltage by the interacting currents. This effect produced a larger peak current in the first inductor at $t \sim 1100 \mu s$. Unfortunately, there were not enough data channels to monitor a complete set of electrical parameters for the power supply and their interaction with the plasma load.

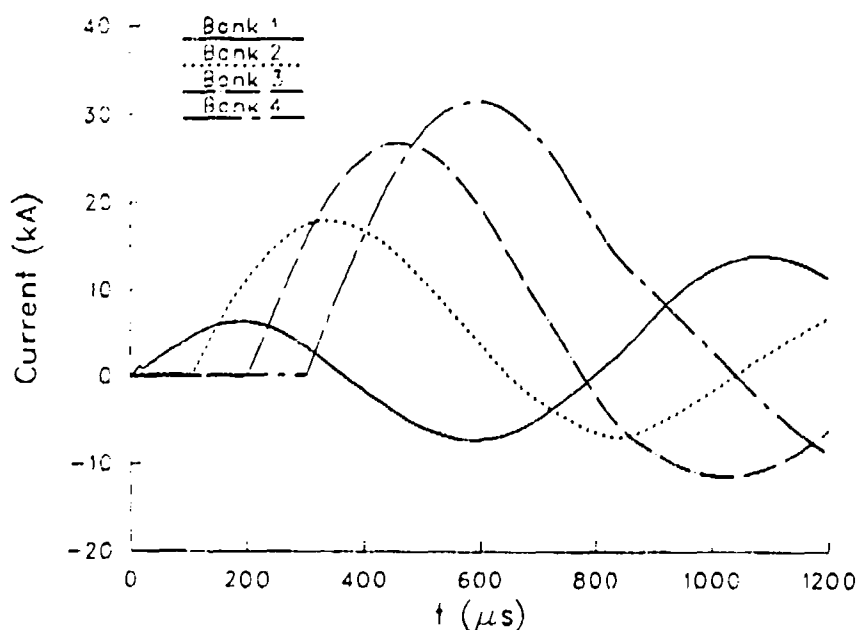


Figure 4. Four Measured Module Inductor Currents as a Function of Time for Shot 8.

The total measured arc current is shown in Fig. 5. The current waveform has a rise-to-peak of approximately $450 \mu s$. The inflection points occurring every $100 \mu s$ are indicative of the triggered modules supplying current to the load. The final pulse width is about $850 \mu s$. The small modulation in the load current for early times has been observed previously during power-supply characterization tests with fixed-load impedances. The amplitude of the modulations can be controlled by adjusting the load impedance. Exact calculation of this effect is impossible mainly because of the undeterminable, distributed stray capacitances and inductances in the pulsed-power supply. However, an excellent description of such phenomena and their relation to measured transient data can be found elsewhere (Burden and Shear 1969). In summary, it has been found when the load impedance is large compared to the module impedance, the load current tends to have many, small-amplitude oscillations

superimposed on the load-current waveform. Such an effect also occurs, as seen in Fig. 5, for times less than $40 \mu s$, when the plasma arc is initiated. When a relatively small impedance is used for the load, as is the case when the current rises to a large level ($t > 200 \mu s$), very few, smaller-amplitude oscillations appear.

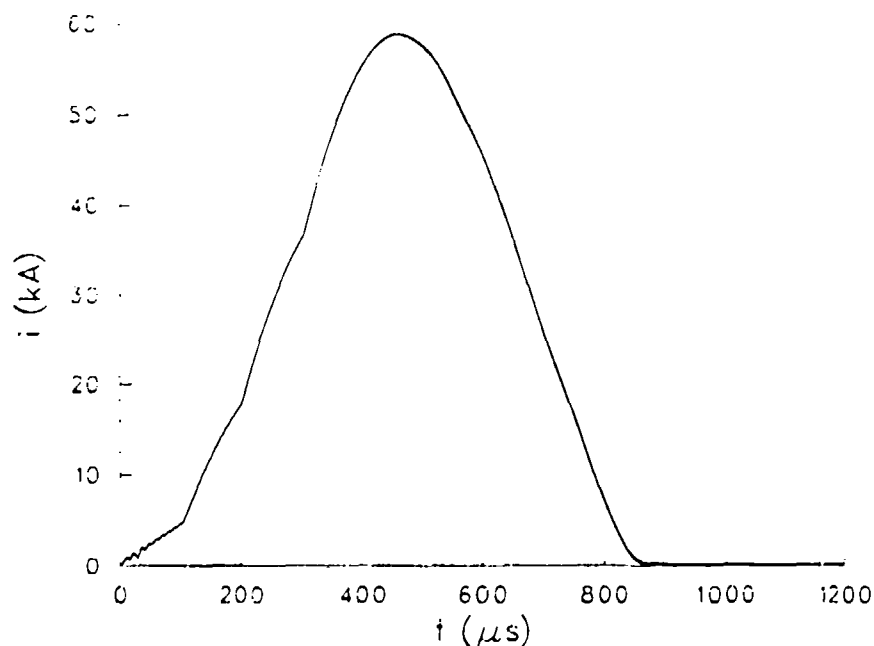


Figure 5. Measured Plasma Arc Current as a Function of Time for Shot 8.

Figure 6 shows a trace of the measured voltage for Shot 8. This voltage includes the capillary resistive and inductive terms. The first $18 \mu s$, during which peak voltage reaches $4.5 kV$, corresponds to vaporization of the aluminum wire. For times less than $100 \mu s$ and greater than $18 \mu s$, the voltage waveform reveals several small oscillations. These oscillations occur for the same reasons as those discussed for the arc current in Fig. 4 and, to a lesser extent, because of the early, time-dependent formation of the plasma. For the remaining pulse duration, the voltage drop roughly follows the shape of the current pulse, with some fine structure appearing in the waveform after peak current. The capillary voltage drop, V , was obtained by subtracting the capillary inductive term $L_{cap} \frac{di(t)}{dt}$, and the steel-anode resistive term, $R_{anode}i(t)$, from the measured anode-to-housing voltage drop as a function of time. Impedance-bridge measurements of the capillary inductance (L_{cap}) and anode resistance (R_{anode}) were made at a frequency of $1 kHz$, and are $101.5 nH$ and $1.75 m\Omega$, respectively. The inductive-voltage term contributes less than 3% to the total measured voltage and is largest at early times. The resistive contribution is slightly larger, about 5%, and is greatest at peak current.

Figure 7 displays the pressure trace for Shot 8 as a function of time. It should be recalled

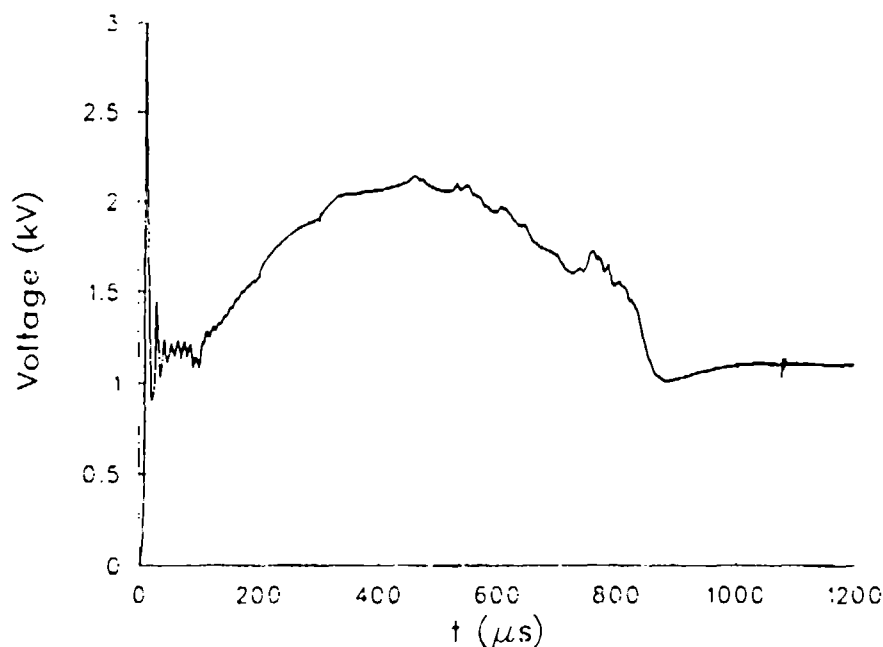


Figure 6. Measured Anode-to-Housing Voltage Drop as a Function of Time for Shot 8.

that this pressure, denoted by P_p , was measured at a point 17 mm from the anode end of the capillary. The pressure waveform is similar in shape to the current waveform but reaches its peak slightly later in time. Again, the inflection points which occur at 100 μs intervals are indicative of current supplied to the plasma load by the three remaining modules. Closer inspection of the data reveals a slight time delay between the current and pressure inflection points. This difference results from several effects. Foremost, the gage has a published response of 1.5 μs and the thin polyethylene wall between the gage head and capillary wall will no doubt increase that value. Furthermore, the plasma may exhibit some time-dependent behavior, especially with rapidly varying di/dt in the circuit. For this shot (Shot 8) the time delay between the current and pressure inflection points was 4 μs for early times but on Shot 4, which had a much smaller peak current and pressure, a 10 μs delay was observed. These values are consistent with the effects mentioned above.

Ground potential, and therefore the reference for the oscilloscope, can shift due to small currents flowing in the inductance and resistance of the ground connection. As a consequence, pulsed signals can converge to nonzero values for long times. In order to verify that the pressure signal returned to the pre-shot zero baseline, we extended the measurement for one shot (Shot 4) long after the pulse-width of the current. In this measurement the transient recorder acquired nearly 8000 μs of data and the pressure waveform was found to approach to zero at 8000 μs .

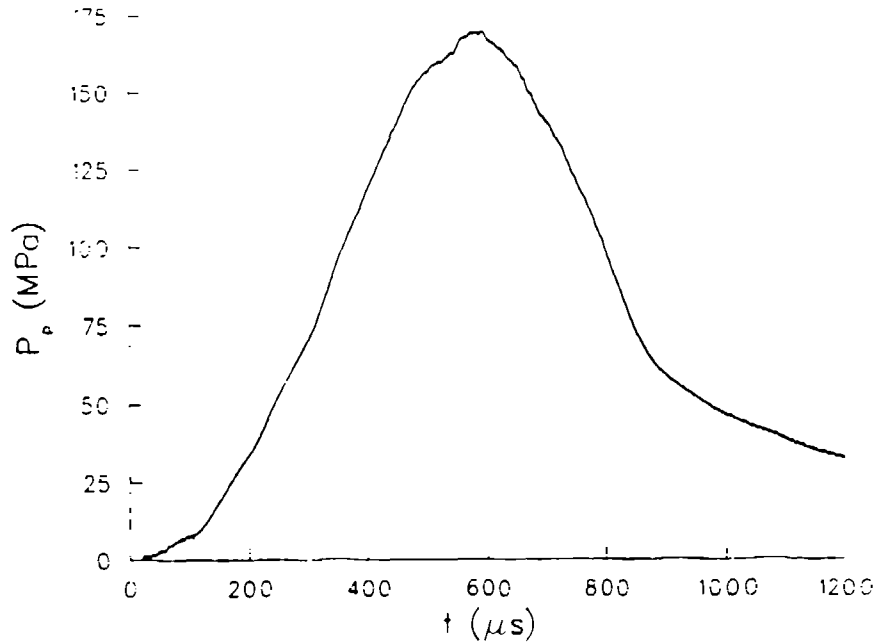


Figure 7. Measured Pressure as a Function of Time for Shot 8.

Perhaps, however, the most interesting regime for examining both the accuracy and acquisition of the pressure data is the initiation phase of the plasma discharge. The fine cylindrical aluminum wire used to initiate the plasma is exploded by the passage of the current pulse produced by Bank 1. This method of plasma initiation is similar to experiments performed previously utilizing exploding-wire phenomena. With wire diameters on the order of 0.1 mm and available energies larger than 5 J/cm , a nearly cylindrical shock wave system is produced (Bennett 1959). The system is fairly complex; however strong-shock, similarity flow theory (Lin 1954) has been found to describe the trajectory of the experimental shock wave and can be used to estimate the peak pressure when the plasma is initiated. In the strong-shock approximation it is assumed that the energy is deposited instantaneously. Uniform atmosphere surrounding the wire is assumed to consist of perfect gas with constant heat capacity. In our experiments energy deposition is not instantaneous and, in fact, extends over a period an order of magnitude longer in duration than that observed in exploding wire experiments (Burden and Shear 1969). Therefore, similarity flow theory should yield an upper limit for the pressure produced in the capillary during arc initiation and is given by,

$$P_{ssf} = \frac{0.216 \mathcal{E}_w}{\ell r_{bi}^2}$$

The energy deposited in the conducting wire, \mathcal{E}_w , is the value taken when the capillary voltage reaches a maximum. At this time the wire conductivity is at a minimum. Thereafter, the

air becomes increasingly ionized and relatively more energy is deposited in the column of air surrounding the remaining metal wire.

The data for Shots 4, 6, 7, and 8 were used to calculate the pressure after wire vaporization. In all tests the calculated pressure overestimated the measured pressure by a factor of about 5 at low energies (less than 1 J/cm) and about 2 at the larger deposited energies ($\sim 3 \text{ J/cm}$). The recorded pressure pulse from wire vaporization peaks $5\text{-}10 \mu\text{s}$ after the wire exploded. This observation is consistent with the development of a cylindrical shock-wave. However, the observed pulse duration is an order of magnitude longer than strong-shock theory would suggest. The differences in both time and magnitude between the calculated and measured initiation event are largely attributable to the gage response (see discussion in the previous paragraphs) and calibration (see discussion in Sec. 5. 4). Further differences can be accounted for by deposition of nonconstant wire energy in a finite time. Most important, is the absence in the pressure signal of noise induced from capacitor bank trigger pulses and circuit transients during wire explosion. This final point gave us confidence that the signal recorded was an accurate representation of the transducer output.

A summary of the experimentally measured parameters for all the shots is shown in Table 2. Included are the current, i_{pk} , in Column 2; the resulting values for the capillary voltage, V , with corrections for the inductive and resistive terms in Column 3; the value of the capillary pressure, P_p , in Column 4; and the time, $t_{i_{pk}}$, at which these data are obtained in Column 5. The next two columns show the value of the peak pressure, P_{pk} , and the time at which peak pressure occurs, $t_{P_{pk}}$, respectively. The last two columns list the measured values for the initial capillary radius, r_{bi} , and the final capillary radius, r_{bf} .

Table 3 summarizes additional, relevant parameters obtained from the measured electrical data. It should be noted that there appears to be a time correlation among the peaks of the voltage, power, current, and pressure. The peak voltage across the capillary occurs first, followed by the peak in the arc current roughly $50\text{-}75 \mu\text{s}$ later. Because of the oscillatory nature of the discharge, peak power occurs a few microseconds before peak current. Peak pressure follows peak current by approximately $100 \mu\text{s}$. Contrary to common assumptions that capillaries of this type operate in the steady-state regime, the measured plasma data appear to exhibit a substantial amount of time dependence. This point will be further discussed in the following pages.

Table 4 presents a summary of results calculated from various measured electrical and physical data. The change in capillary radius, Δr , listed in Column 2, was obtained from the difference of the final and initial values for the capillary radii (see Table 2). The capillary mass loss was calculated from that difference and the density of polyethylene (950 kg/m^3).

Table 2. Summary of Measured Data

Shot	$i_{pk}(kA)$	$V(volts)$	$P_F(MPa)$	$t_{i,pk}(\mu s)$	$P_{pk}(MPa)$	$t_{P,pk}(\mu s)$	$r_{bi}(mm)$	$r_{bf}(mm)$
1†	7.50	1443.5	*	407	*	*	†	†
2	10.5	1440.3	*	383	34.0	516	3.175	†
3†	23.8	1483.4	60.6	480	67.4	593	†	3.302
4	31.9	1597.7	83.1	480	91.6	566	3.365	3.454
5	41.9	1777.4	125.4	473	141.6	563	3.454	3.543
6	45.3	1832.1	129.1	474	146.0	572	3.568	3.670
7†	47.4	2024.5	124.1	453	148.4	609	3.683	3.797
8	58.7	2034.7	143.9	460	169.7	589	3.835	3.962

† Not measured.

* Pressure measurements not valid.

† Soldered fiber-optic holes had blown out.

Table 3. Peak Data

Shot	$V @ t$		$P_D @ t$		$i @ t$		$P_p @ t$	
	(kV)	(μs)	(MW)	(μs)	(kA)	(μs)	(MPa)	(μs)
1	1.453	366	10.91	392	7.5	407	*	*
2	1.510	274	15.37	349	10.5	383	34.0	516
3	1.552	356	35.42	471	23.8	480	67.4	593
4	1.653	372	51.65	450	31.9	480	91.6	566
5	1.837	385	74.84	459	41.9	473	141.6	563
6	1.910	399	83.78	456	45.3	474	146.0	572
7	2.021	389	96.71	460	47.4	453	148.4	609
8	2.040	463	120.0	463	58.7	460	169.7	589

* Pressure measurements not valid.

Table 4. Summary of Energy-Conversion Data

Shot	$\Delta r(\mu m)$	$\Delta m_{cap}(mg)$	$\mathcal{E}_D(kJ)$	$\frac{\mathcal{E}_D}{\Delta m_{cap}}(\frac{MJ}{kg})$	$R_{min}(m\Omega)$	$\eta (\%)$
1	20.1 [†]	23.4 [†]	5.3	224.9 [†]	189.9	45.3
2	27.5 [†]	32.3 [†]	7.3	225.3 [†]	134.7	68.6
3	56.3 [†]	66.9 [†]	15.0	224.7 [†]	62.2	82.6
4	88.5	109.7	21.4	194.4	49.8	81.1
5	178.0	113.2	29.8	263.8	41.7	83.1
6	203.0	133.5	34.1	255.4	40.1	72.2
7	228.0	155.0	37.4	241.4	41.7	71.9
8	254.0	180.0	47.0	261.4	34.0	73.6

[†] Extrapolated from results on Shots 4-8.

The total energy deposited in the capillary, \mathcal{E}_D (Column 4), was obtained by integrating the product of the measured capillary voltage and current over the width of the current pulse. The ablation coefficient for the polyethylene capillary was taken to be the ratio of deposited energy to mass loss and is shown in Column 5.

We should finally point out that, for a power supply delivering energy to a load, the load impedance plays a crucial role in determining the amount of energy transferred. In electrothermal guns, we are concerned with maximizing the energy dissipated in the plasma. Typically, an impedance can be found which will maximize the amount of energy transferred and hence the transfer efficiency η . As the load impedance exceeds that for maximum efficiency, the amount of transferred energy steadily decreases; for load impedances even slightly less than that at maximum efficiency, the amount of energy transferred can be greatly decreased. This effect is particularly pronounced with a plasma load since the plasma resistance becomes smaller for larger currents. Even in the relatively short series of firings discussed here, the effect of load resistance on the transfer efficiency can be seen. The minimum of $V(t)/i(t)$ for each shot was used to calculate the minimum plasma resistance, R_{min} , listed in Column 6 of Table 4. Low-current shots produce a fairly high-resistance load for which the transfer efficiency is found to be less than 70% (Shots 1 and 2). For a load resistance below 40 $m\Omega$, the transfer efficiency also begins to decrease. For this power supply, maximum efficiency for energy transfer is near 85% and occurs for a load impedance in the range of 40-65 $m\Omega$.

5.4 Pressure-Gage Calibration. In our early attempts to measure the plasma pressure, a small, silicone-grease-filled hole was used to communicate pressure in the volume of the capillary to the pressure transducer. However, this idea was quickly abandoned as the silicone grease failed to insulate the gage from the high, pulsed electrical current. An alternative method was to simply insert the gage under vacuum into a shallow cavity machined in the outer capillary wall, thereby leaving a thin section of polyethylene between the gage head and the inner surface of the capillary wall. The transducer had a flat, circular steel diaphragm welded to the transducer casing. When mounted radially, the polyethylene wall then projected a nonuniform cross section to the gage head, one which was thin at the center of the gage and thicker at the ends.

To evaluate the transducer system as completely as possible, it was decided to perform the gage calibration *in situ*. To obtain pressures comparable to the electric-discharge experiments, a fluid-and-piston arrangement was employed. A short section of barrel fabricated for calibration purposes was joined to the capillary using a galvanized pipe coupling. A second Kistler pressure transducer (Model 217C), used for a reference measurement, was mounted in the standard, ballistic orientation near the muzzle end of the calibration barrel. A polyethylene rod, drilled to the depth of 60.9 mm, was used to form the capillary. A steel piston with three O-rings around the piston shaft was mounted on four guide pins and was free to slide into the muzzle end of the calibration barrel. Diffusion-pump oil was used as the compressing fluid. A stand was constructed by which steel disks could be dropped onto the steel piston. The weights (30 kg maximum), which were attached to an aluminum plate, were guided by four steel wires. The capillary and calibration barrel were assembled in the aluminum housing and positioned upright at the bottom of the drop stand. To ensure that initial air was trapped in the compressing fluid prior to insertion of the piston and dropping the weight, the piston had a small threaded hole through the shaft by which trapped air could be released. Once the air was sufficiently removed from the barrel and the piston seated to the proper depth, the through-hole was sealed. The weights were released one meter above the piston, subsequently compressed the fluid in the capillary and the calibration barrel, and thereby generated the desired pressure pulse. Peak pressures similar to those in the electrical discharges were obtained, although pressure rise times were on the order of a few milliseconds. This type of measurement was repeated for each capillary diameter fired, and for various sizes of drop weight. A typical set of pressure traces is shown in Fig. 8. It can be seen from Fig. 8 that both transducer signals cross at early times. This behavior is partially due to the propagation delay time of the pressure wave in the fluid column.

The ratio of the pressure recorded with the reference gage to the pressure recorded by the capillary gage was taken to be the calibration factor and, as indicated, was determined for

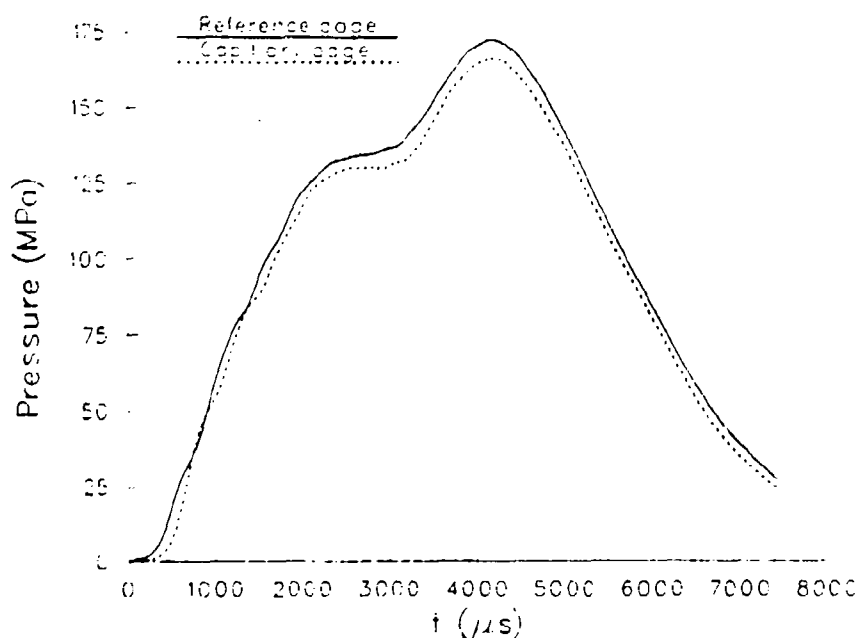


Figure 8. Reference Pressure and Capillary Pressure as a Function of Time.

each capillary diameter tested. The tests which yielded the largest peak pressures were used in determining the calibration factor. Similar calibration curves were obtained regardless of the peak pressure for a given capillary diameter. The calibration curves can be separated into two distinct regions: positive dP/dt (rising pressure) and negative dP/dt (falling pressure). Curves for the falling pressure data are shown in Fig. 9. The calibration factor is fairly constant, particularly for pressures greater than the yield strength of polyethylene (31 MPa). Furthermore, deviation from the reference transducer reading is on the order of a few percent for the larger diameters and 15% for the smaller capillary diameters. The rising pressure data are shown in Fig. 10. These data exhibit the same behavior, except for some oscillations occurring at early times. The nature of this behavior can be attributed to the inadequate seals and joints used in the barrel assembly. During the initial pressure rise, the fluid probably filled voids formed during assembly of the capillary to the barrel.

Of particular interest is the calibration test for the 6.731 mm diameter capillary. On that test the drop weight bounced on the piston producing a double-peaked pressure pulse for which the second pulse was initiated before the first could fall to zero. It appears from these data that once the initial pressurization of the fluid in the capillary column was completed (at 80 MPa), the calibration factor remained fairly constant at 0.830 with a deviation of $\pm 3.4\%$, even for pressures which subsequently fell below 80 MPa.

A calibration test was also done using the 7.137-mm diameter capillary; as an expediency,

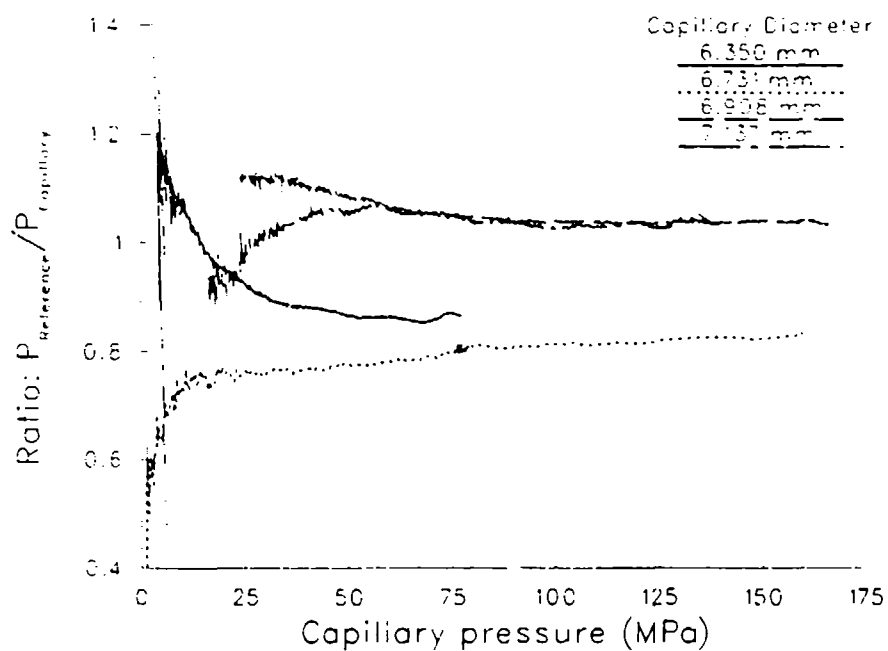


Figure 9. Calibration Factor as a Function of Measured Capillary Pressure. Data are for falling pressure.

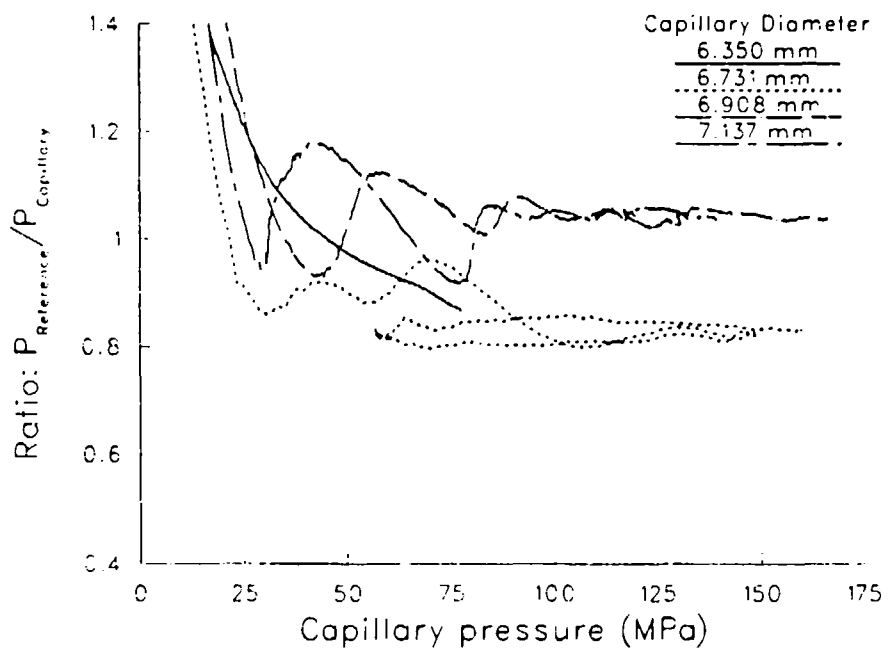


Figure 10. Calibration Factor as a Function of Measured Capillary Pressure. Data are for rising pressure.

Table 5. Summary of Calibration Constants for the Capillary Gage

Capillary Diameter (mm)	Wall Thickness @ the Gage (mm)	Calibration Factor
6.350	1.77	0.863
6.731	1.58	0.823
6.908	1.49	1.044
7.137	1.38	1.035

the capillary gage was installed under atmospheric conditions to facilitate the tests. There was no appreciable deviation in the calibration factor for pressures greater than 75 *MPa*. However, the oscillations appearing at low, rising pressure were somewhat erratic.

Data for the largest capillary diameter tested (7.67 *mm*) are not shown. The peak pressure attained using that diameter (180 *MPa*) was sufficient to burst the galvanized pipe coupling that joined the capillary to the calibration barrel. However, the calibration factor obtained prior to failure did not deviate significantly from that obtained using the 6.908 and 7.137 *mm* capillary diameters.

It should be noted that the form and duration of the pressure pulses are not identical to those generated in the electrical-discharge experiments. In the electrical firings, one end of the capillary was open and the other sealed with the steel anode. In the calibration experiments, both ends were, to a great extent, closed. Also, the calibration tests were performed at room temperature whereas the electrical tests produced elevated wall temperatures. High temperatures should cause the polyethylene to yield at a reduced pressure allowing the gage to follow the plasma pressure more closely as a function of time.

The capillary gage calibration factors were taken to be a best-fit, constant-value for pressures greater than the yield strength of polyethylene (34 *MPa*). An average of the rising and falling data was used, and are listed in Table 5. As can be seen from the table, wall thicknesses greater than 1.58 *mm* cause an overestimate in the actual pressure by about 15%, while thinner wall thicknesses yield underestimated pressures by only about 4%.

6. CALCULATIONS AND COMPARISON WITH EXPERIMENT

We now turn to undertaking some specific calculations with both the steady-state and time-dependent models. In all cases we attempt to carry out calculations which allow us to compare the results with experimental data. Considerable discussion will be presented indicating the extent to which the theory and experiment agree, as well as attempting to

interpret physically the results.

6.1 Steady-State Calculations. In PZ1 we exercised the steady-state, isothermal model to compute plasma properties for five of the shots discussed in the previous section. The shots selected for analysis were those for which valid pressure data were obtained, i. e., Shots 2, 4, 5, 6, and 8. The calculations were carried out using as input the peak current obtained in each of the five shots. A comparison of the theoretically obtained voltage drop, V_{th} , measured across the length of the capillary, was also compared with that obtained experimentally and given here by V_{ex} . The voltage can be calculated from the simple and obvious formula

$$V_{th} = i\ell/(\pi r_b^2 \sigma). \quad (47)$$

We now undertake similar calculations using the updated steady-state model. The principal difference between these calculations and those reported in PZ1 is that the present model includes the nonideal effects discussed in Sec. 2. Results of the calculations are shown in Table 6. Most of the results are self-explanatory and need little discussion. The radius r_b was obtained from the average of r_{bi} and r_{bf} indicated in Table 2. The capillary length, ℓ , was in every case equal to 6.09 cm.

The quantity \mathcal{P}_D , shown in Column 7, represents the power dissipated in the capillary due to the finite resistance and is given by $\mathcal{P}_D = i_{pk} V_{th}$. This quantity is important in assessing the capillary performance because, in the steady state with no heat loss to the walls, this energy is equivalent to that which flows past the capillary exit.* Thus, typically, for time scales of the order of a few milliseconds, one can use the capillary to furnish energy of the order of several tens of kilojoules. The quantity \tilde{Z} in Column 8 represents the ratio of the total number of ions in the plasma to the total number of heavy particles. Consequently, this number gives some indication of the extent of ionization and increases with increasing current and temperature (Column 6). The parameter \dot{r}_b in Column 9 gives the recession rate of the solid surface and m , in Column 10, the steady-state mass contained in the capillary. Finally, $\langle P \rangle$ represents the pressure averaged over the capillary length, and $\langle \gamma_n \rangle$ represents the similarly averaged nonideal parameter which measures roughly the ratio of kinetic to potential energy in the plasma. Various, nearly similar, definitions of the nonideal parameter exist and we have used the relation

*If the energy passing the capillary exit per unit time is calculated in the isothermal, steady-state model, it will be found to differ from the dissipated energy by a slight amount equal to the kinetic energy of the gas products. The reason, of course, is that the kinetic energy was neglected relative to the internal energy in the approximations leading to the development of the model. We are grateful to Dr. Jad H. Batteh who pointed out to us the existence of and reason for this discrepancy.

Table 6. Calculations with Isothermal, Steady-State Model and Comparison with Experimental Results

Shot #	i_{pk} (kA)	r_b (mm)	V_{ex} (volts)	V_{th} (volts)	T (eV)	\mathcal{P}_D (MW)	\dot{Z}	\dot{r}_b (cm/s)	m (mg)	$\langle P \rangle$ (MPa)	$\langle \gamma_n \rangle$
2	10.5	3.18	1440	1339	1.83	14.1	0.39	3.74	0.68	18.4	0.26
4	31.9	3.41	1598	1926	2.61	61.4	0.71	9.64	1.43	58.8	0.27
5	41.9	3.50	1777	2113	2.84	88.5	0.76	12.4	1.78	78.3	0.27
6	45.3	3.62	1832	2109	2.87	95.5	0.77	12.8	1.88	78.5	0.27
8	58.7	3.90	2035	2188	3.03	128.4	0.81	15.0	2.28	89.0	0.26

$$\gamma_n = \frac{e^2(n_e + n_i)^{1/3}}{4\pi\epsilon_0 kT}. \quad (48)$$

As was pointed out previously, values of this parameter larger than about 0.1 indicate that Coulomb interactions and the resulting nonideal effects should not be neglected.

Comparing the voltages V_{ex} and V_{th} for the various shots, we see that the agreement is fairly good; maximum deviations are about 20%. We should also point out that the results are not vastly different from those obtained via the model in PZ1. Voltages are slightly higher for the computations here since the nonideal effects lead to a reduction in the electrical conductivity. Experimental voltages are slightly smaller than those in PZ1 because corrections for anode resistance and capillary inductance have now been included as discussed in Sec. 5. For none of the quantities computed in the table, however, did we observe differences larger than about 10% from those calculated in PZ1. This conclusion is perhaps surprising since, at a given temperature and pressure, nonideal effects can have a much more significant impact on the conductivity. In the problem at hand, however, in which all the variables are nonlinearly coupled, a reduction in the conductivity because of nonideal interactions leads to an increase in resistive heating. This increase is followed by a rise in temperature which tends to bring the conductivity back up. Thus, the overall effect is not so significant as might be expected *a priori*.

In PZ1 we also investigated a model which was steady state, but in which the isothermal approximation was not assumed. In other words, the variables which were assumed to be position independent in the previous section, were allowed to vary. In the present work, we have not developed such a model explicitly, but rather have obtained steady-state results by

relaxing the time-dependent calculations for a specific current until nearly steady behavior was observed. We discuss now some of the results of a calculation undertaken for Shot 8 (see Table 6). This calculation was performed primarily to examine the validity of the isothermal approximation.

The initial conditions for the calculation were taken to be the steady-state values obtained via the isothermal model. These variables will not satisfy the equations of the more general model initially, and will evolve in time until a new steady solution is reached. A comparison of the two steady solutions should then provide an indication of how accurate the isothermal model is.

For the isothermal case, we showed in the previous section that no steady-state solution existed for $w(z = \ell)$ greater than C_{s0} where C_{s0} represented the isothermal sound speed. For $w(z = \ell) = C_{s0}$, the flow is choked and it is easy to show that the breech and exit pressures must satisfy

$$P_0 = P(z = 0) = 2P(z = \ell). \quad (49)$$

Under conditions which are not isothermal, the sound speed is more difficult to compute, and we have for simplicity used Eq. (49) to supply the additional boundary condition required. The sound speed at the point $z = \ell$ has been estimated in our calculations from the very approximate expression

$$C_S = (\gamma_{eff} P / \rho)^{1/2}, \quad (50)$$

where γ_{eff} is the effective adiabatic exponent or specific-heat ratio for the plasma given by (Zeldovich and Raizer 1966)

$$\gamma_{eff} = 1 + P/(\rho E). \quad (51)$$

Equation (50) is known (Tidman and Goldstein 1985) to produce an estimate of C_S which is slightly higher than that produced by the more rigorous expression, namely,

$$C_S = \left(\frac{\partial P}{\partial \rho} \right)_S^{1/2}, \quad (52)$$

with the subscript S denoting partial differentiation at constant entropy.

Shown in Figs. 11 and 12 are pressure and temperature profiles obtained from both the isothermal model and the more general model discussed above. Results are plotted as a function of the dimensionless distance $\xi = z/\ell$. As can be seen, the pressure in the arc agrees to within, at worst, about 15% everywhere; the temperature is in somewhat better agreement. Presumably, the slight drop in temperature with increasing ξ results from a greater percentage of the total energy in the arc being associated with kinetic energy of the gas products as they are accelerated near exit. Similar observations were noted in PZ1. The load voltages predicted by the general and isothermal (see Table 6) models were 2047 and 2188 V, respectively. Similarly reasonable agreement has been found for other variables and other shots and we conclude that the isothermal model can be used reliably for predictions in cases for which the flow is steady and for which extreme accuracy is not required.

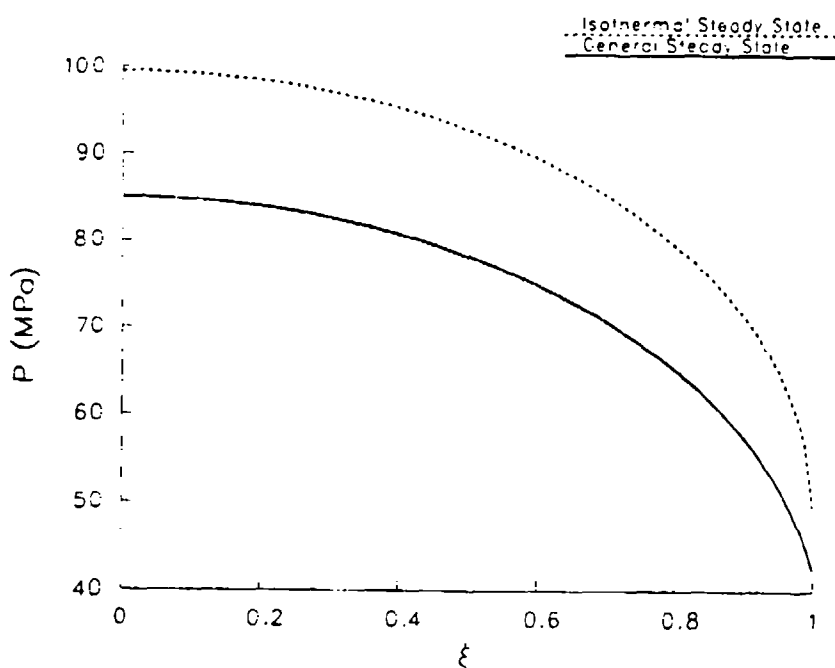


Figure 11. Comparison of Steady-State Pressure Profiles in the Isothermal and General Models for Shot 8.

6.2 . Time-Dependent Calculations. In addition to the steady-state calculations described above, we have also undertaken a number of time-dependent calculations with the more general model. The purpose of these calculations was to compare with time-dependent experimental data for the shots discussed in the preceding subsection. It is necessary for these calculations to input the current $i(t)$ as a function of time. This current was obtained from experiment (see, e.g., Fig. 5) and then fitted to a sixth-order polynomial in time. Such a fit was found to give an accurate representation of the actual measured current except at the very end and the very beginning of the current pulse. These extremes were omitted from

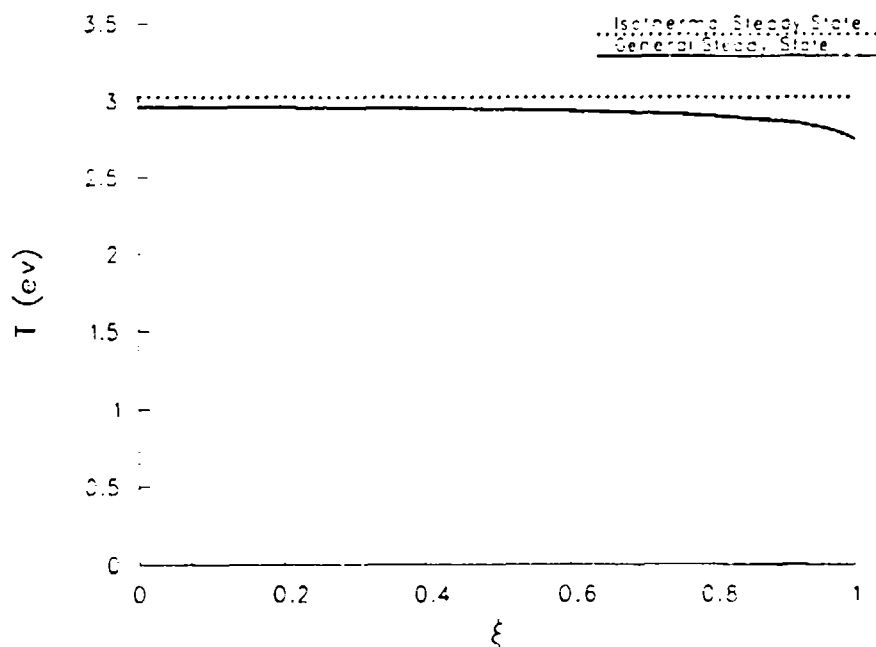


Figure 12. Comparison of Steady-State Temperature Profiles in the Isothermal and General Models for Shot 8.

the calculation anyway, since we selected for analysis a region about peak current for which the pressure measurements were felt to be particularly accurate.

For all these calculations, the boundary condition at exit was taken to be that given in Eq. (49). When this condition was applied, we generally found that the exit speed of the gas products was slightly less than our estimate of the sound speed at exit obtained from Eq. (50). The initial conditions employed in each case were the steady-state values of the various parameters obtained at a value of the current equal to that which we chose to be the initial value in the pulse described above. These values were obtained by running the time-dependent code at the initial current until a steady state was achieved, and then allowing the current to vary.

We now discuss some of the results of the calculations. We will confine our attention to Shots 4 and 8; other cases gave very similar results. We will first discuss some purely theoretical results and then compare with the available experimental data.

Shown in Figs. 13-15 are pressure, velocity, and temperature for Shot 8 at three different times. The only noteworthy aspect of these graphs is the observation that the profiles look reasonably steady; the shapes of the curves hardly change as the current rises from about 36 kA at 300 μ s to a peak of about 58 kA at around 460 μ s, and then drops to about 26 kA at 700 μ s. Further evidence of the steady behavior can be seen from data in Table 7 in which

are shown in Columns 3 and 4 the power dissipated in the arc at the time in question, \mathcal{P}_D , and the power passing the capillary exit plane, \mathcal{P}_F . The latter quantity was calculated from the expression

$$\mathcal{P}_F = A[\rho w(E + w^2/2) + Pw]_{\xi=1}. \quad (53)$$

As suggested previously, one would expect results in Columns 3 and 4 to be equal in steady state. Actually the results agree to within, at worst, about 5%.* Also shown in the table in Column 5 is the estimated sound speed at the exit plane calculated from Eq. (50) and, in Column 6, the exit velocity of the gaseous products. As pointed out, the exit speeds are somewhat smaller than the estimated sound speed.

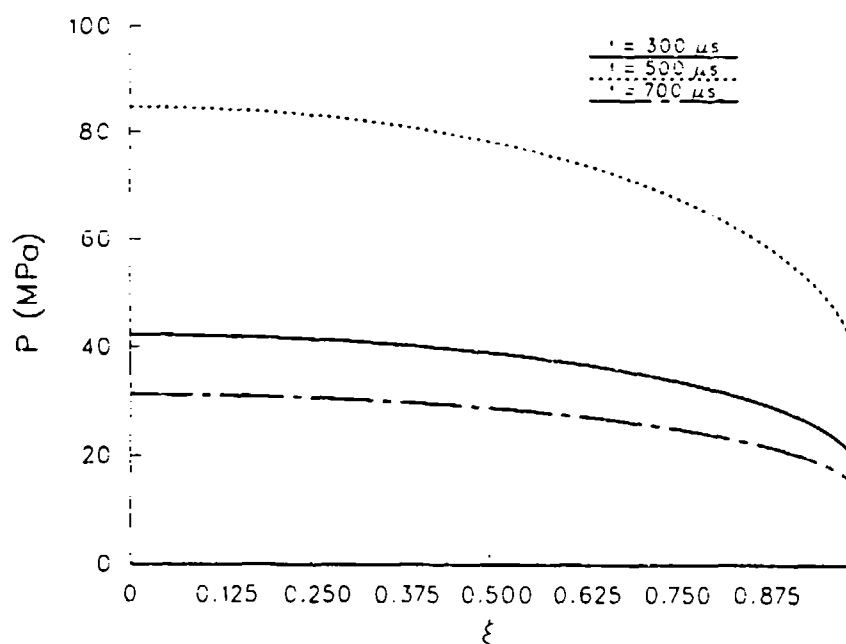


Figure 13. Calculated Pressure Profiles at Several Times for Shot 8.

One of the principal reasons for investigating a time-dependent model was the observation, made by us as well as others, that many of the plasmadynamic variables in these arc-discharge experiments exhibit significant time-dependent behavior. The very early experiments of Ibrahim (1980), for example, indicated that the capillary voltage was not a single-valued function of the current as one would expect for completely steady behavior. Furthermore, it was noted in that work that even more significant time-dependent behavior was observed in other arc variables such as the pressure. The later work by Ruchti and

*We could also compare the mass ablated per unit time with the mass which flows past the exit, as well the momentum flux to the total pressure drop across the capillary. These calculations have in fact been carried out, and the results indicate nearly steady behavior.

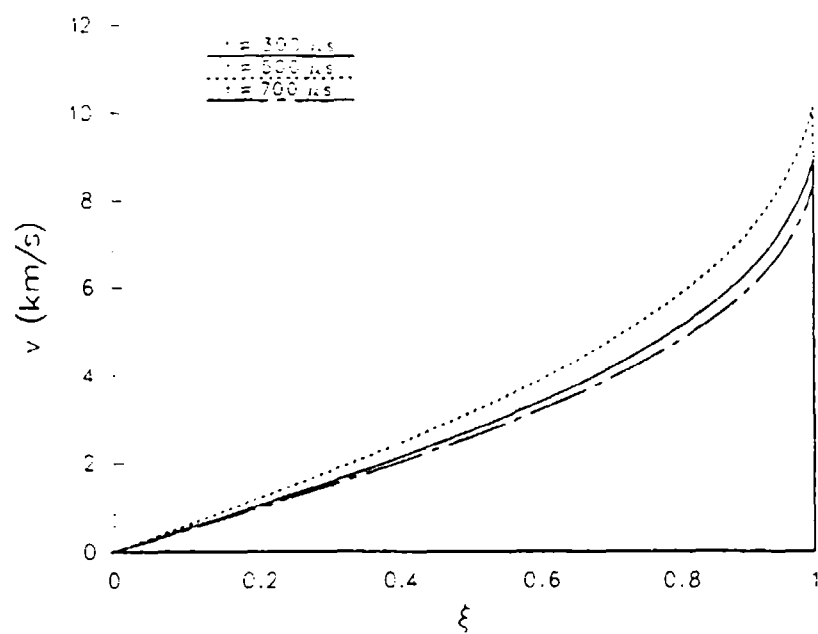


Figure 14. Calculated Velocity Profiles at Several Times for Shot 8.

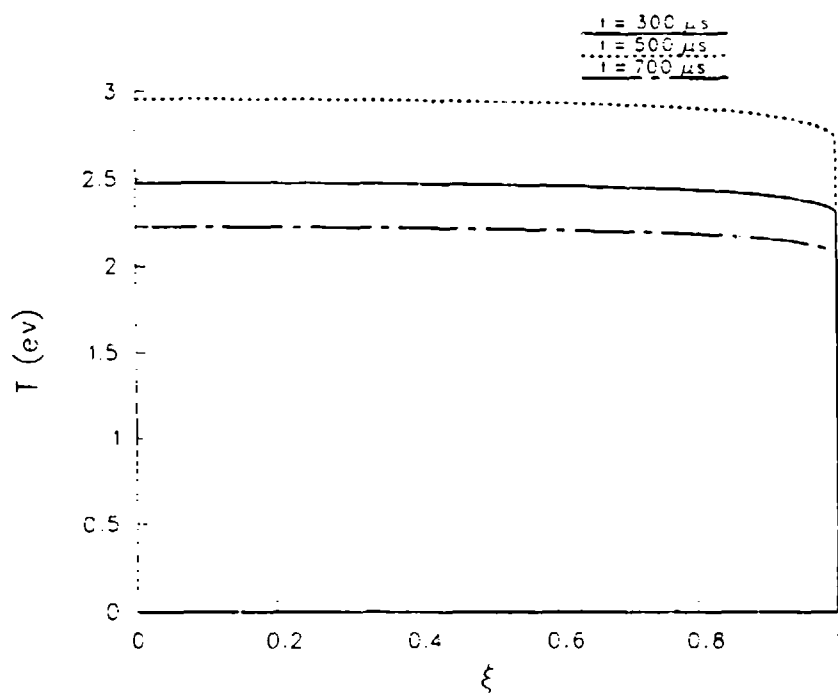


Figure 15. Calculated Temperature Profiles at Several Times for Shot 8.

Table 7. Theoretical Results from Time-Dependent Calculations for Shot 8.

t (μs)	i (kA)	P_D (MW)	P_F (MW)	$C_s(\xi = 1)$ (km/s)	$v(\xi = 1)$ (km/s)
300	36.1	60.7	57.2	9.8	8.8
500	58.3	121.2	121.7	11.1	10.0
700	26.2	38.5	41.2	8.9	8.2

Niemeyer (1978), if examined carefully, also demonstrates substantial time dependence in the measured pressure versus current, with the current reaching peak value considerably prior to the time at which the pressure peaks. Finally, with regard to electrothermal guns, "hysteresis" effects have been observed in voltage-versus-current profiles not only by us but by other investigators at BRL as well (Katulka *et al.* 1990).

In order to compare calculated time-dependent results with experimental data, we have plotted in Figs. 16-19 for both Shots 4 and 8 the experimentally measured conductance and pressure as a function of current. The graphs were plotted only for the time during which the calculations were carried out, i. e., for $200 \mu s < t < 700 \mu s$ for Shot 8, and $300 \mu s < t < 700 \mu s$ for Shot 4. Shown on the same graphs are the calculated results for the appropriate time interval.

In Fig. 16 are the experimental and theoretical values of the conductance for Shot 8 as a function of current. It is evident from the curves that both the experimental and theoretical value of the conductance is, at any fixed value of i , slightly lower when the current is rising than when it is falling. The difference is much more pronounced, however, in the experimental than in the theoretical case. Similarly, shown in Fig. 17, are the calculated and experimental values of the pressure P_p at the point $\xi = 0.28$ (or $z = 17 mm$) as a function of the input current. Here the time-dependent effect is considerably more evident, especially in the experimental data, where the pressure is a factor of two or so higher when i is falling compared to when it is rising. Similar results can be seen for Shot 4 in Figs. 18 and 19.

The slight time dependence in the theoretical results, which arises from the time-varying current, can be described approximately as follows. A small increase in current leads to an immediate increase in Joule heating and a corresponding rise in temperature. Thus, the rate of ablation, which depends primarily on T , also rises with the temperature. The rate of mass loss in the capillary, however, depends not only on T but also varies strongly with the density ρ . Therefore, the rate at which mass flows out the capillary will be lower than

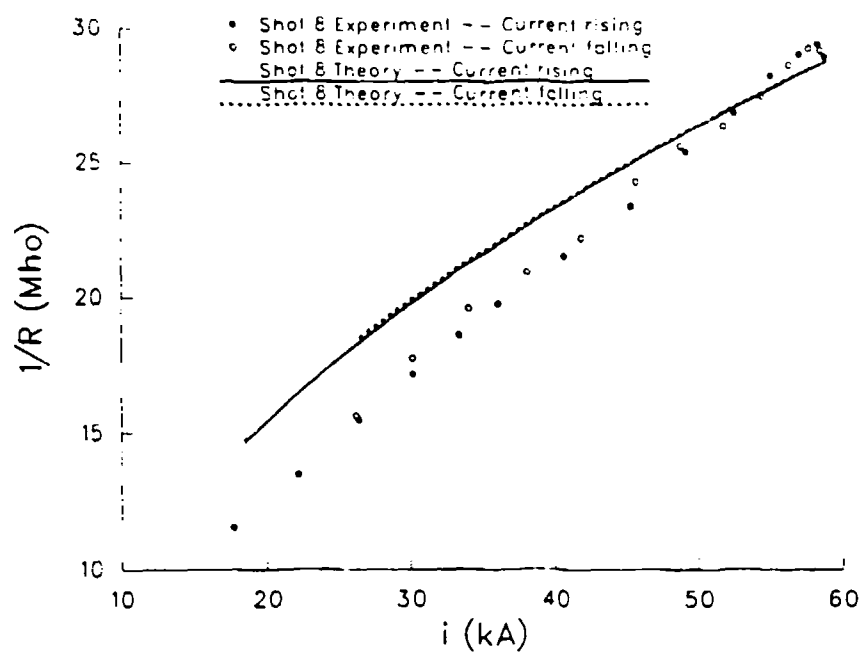


Figure 16. Experimental and Calculated Values of the Conductance as a Function of Current for Shot 8.

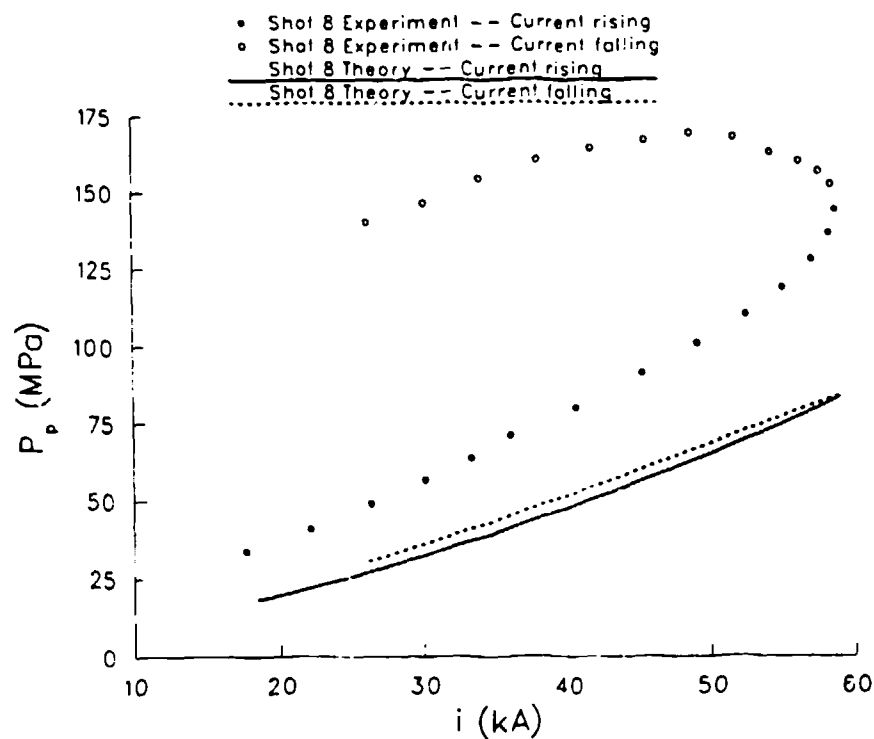


Figure 17. Experimental and Calculated Values of the Pressure as a Function of Current for Shot 8.

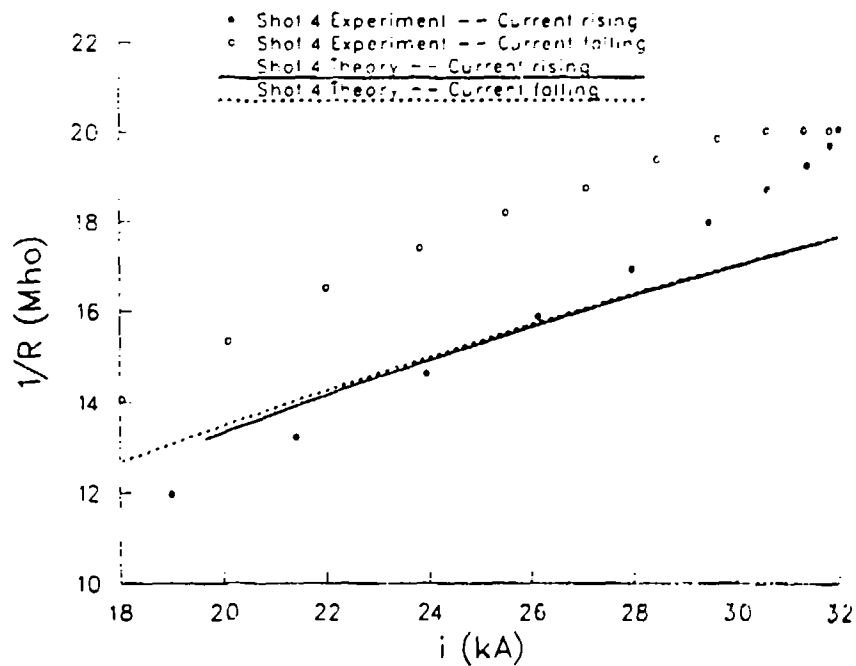


Figure 18. Experimental and Calculated Values of the Conductance as a Function of Current for Shot 4.

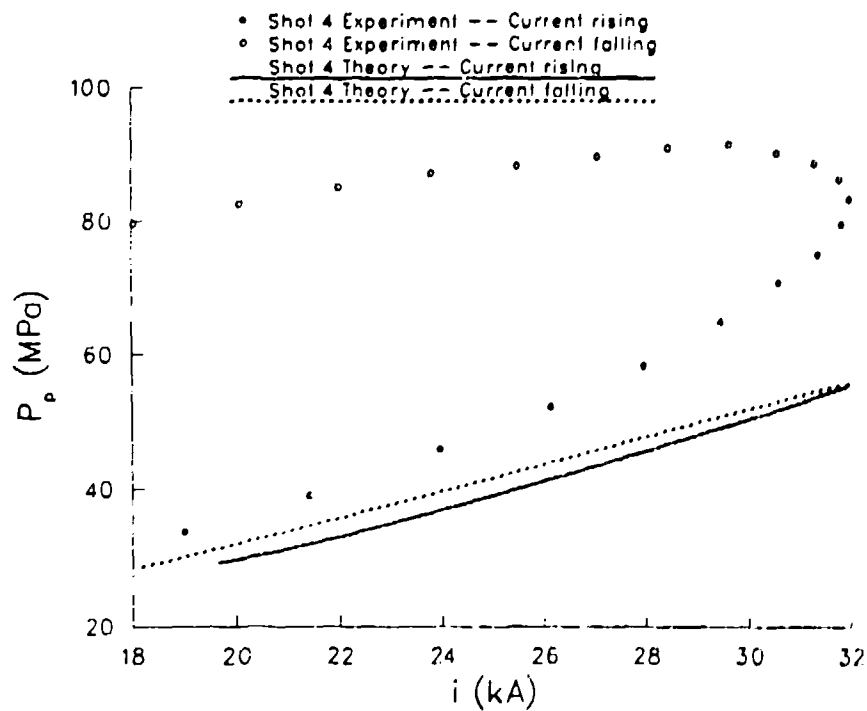


Figure 19. Experimental and Calculated Values of the Pressure as a Function of Current for Shot 4.

the rate at which it increases owing to ablation, and $\partial p/\partial t$ will be positive. As a result, both the density and pressure within the capillary will be lower than under steady-state conditions corresponding to the new T . The reverse explanation is obviously true when dT/dt is negative. Thus, one would expect that the peak in the current i would occur prior to the peak in pressure P , and that the pressure would be lower when the current was rising than when it was falling. Furthermore, since the electrical conductivity increases slightly with increasing pressure (at fixed temperature) in this regime, one also expects the conductance, $1/R$, to be higher at the higher pressures. However, the conductivity is only a very weak function of pressure, so the effect is expected to be very slight as is indeed observed.

It is interesting that the time dependent model predicts trends in the pressure- and voltage-versus-current profiles similar to those seen in the experiments. However, the time-dependent effects are much more pronounced in the experimental data than in the theoretical predictions, especially with regard to the measured and calculated values of the pressure. That there is relatively good agreement between measured and calculated values of the voltage can presumably be ascribed to weak dependence of the plasma conductivity on pressure. The calculations indicate very nearly steady behavior of the plasma properties, and demonstrate that the current indeed varies sufficiently slowly that the plasma properties can follow these changes in a nearly quasi-static manner. In the following section we will attempt to offer some explanations for the significant amount of time dependence observed in the experimental results and indicate some improvements in both the model and experiments which might illuminate our understanding.

0.3 Calculations Employing Measured Pressure as Input. One possibility for the lack of agreement between the experimental and theoretical values of the pressure could be that the exit speed of the gases is not well approximated by the sonic condition. In an attempt to avoid using this assumption, we have undertaken calculations in which the measured pressure was taken to supply the boundary condition needed in the solution of the conservation equations. Predicted values of the voltage across the capillary can then be compared with both the experimental results and the results predicted under the assumption that the flow is sonic at exit.

For simplicity, and since the time dependent calculations have predicted nearly steady behavior, these calculations have been carried out only for the steady state isothermal model. Values of the current were taken from the experimental data at successive values of the time, and the corresponding values of the pressure were used to evaluate the breech pressure P_b which appears in Eq. (37).

Results of the calculation for Shot 8 are shown in Fig. 20 in which are plotted the plasma conductance obtained from the experimentally measured voltage and current, the value obtained via the steady-state model under the assumption that the flow was sonic, and finally the value obtained when the calculation was carried out using the experimental pressure as described above. The results tend to indicate slightly better agreement between theory and experiment for the case in which the pressure was matched than in the case in which the exit flow was assumed to be sonic. As is evident in the figure, and as has been pointed out previously, the voltage or conductance is not very sensitive to the capillary pressure since the plasma conductivity depends primarily on the temperature.

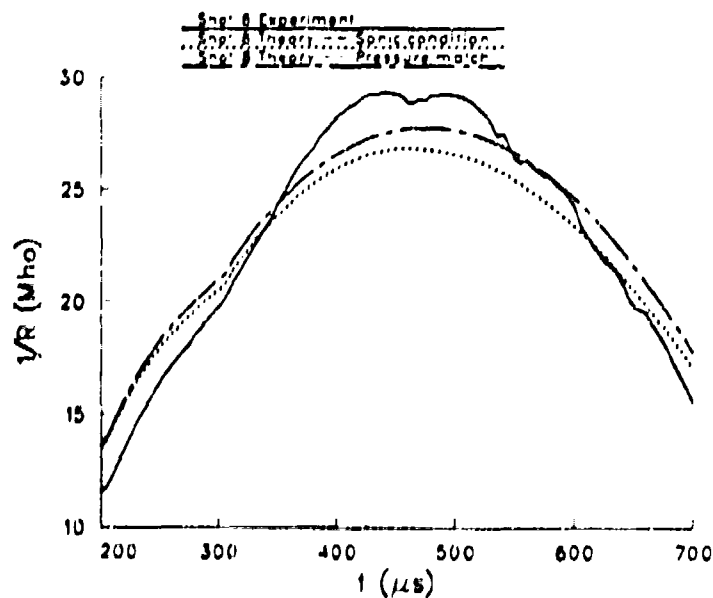


Figure 20. Measured and Theoretical Values of the Conductance for Sonic and Nonsonic Exit-Flow Conditions. The results are for Shot 8.

It is also of interest to determine the extent to which the sonic condition is satisfied when the pressure is matched to experiment in the manner described above. To answer this question we have plotted the Mach number of the gas at exit for the time during which the calculation was carried out. Results are shown in Fig. 21. As is evident, the flow is always subsonic since the Mach number is less than unity. For the first 450 μs or so of the calculation, the gas exits the tube at a roughly constant fraction of the sound speed. Around the time of current peak, however, the Mach number begins to decrease rapidly and drops by a factor of about two during the remainder of the calculation. These results will be discussed in some greater detail in the following section.

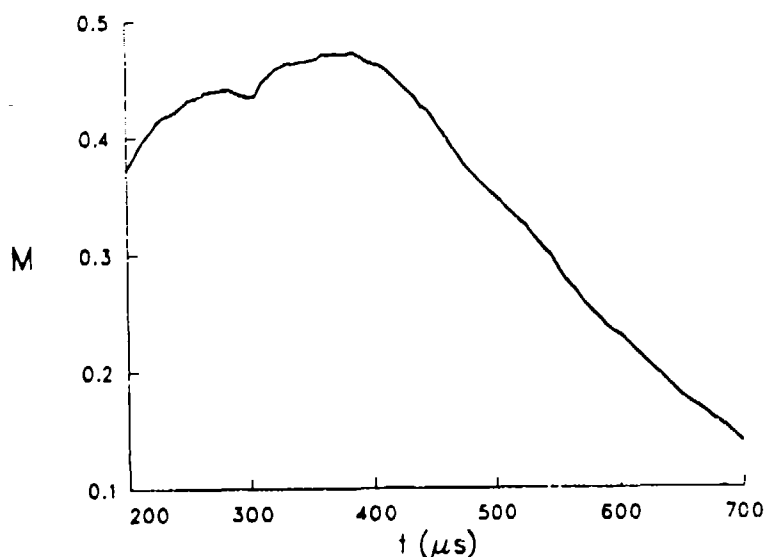


Figure 21. Plasma Mach Number at Exit Plane for the Pressure-Match Calculation.

7. CONCLUSIONS AND DISCUSSION

We have carried out both steady-state and some time-dependent calculations of plasma properties for capillary discharges similar to those which occur in electrothermal guns. Results have been compared with experimental values of the capillary voltage and of the pressure measured at a specific point in the capillary tube. General conclusions obtained from this work can be described as follows:

1. The steady-state, isothermal model, for the assumption that the flow is sonic at exit, gives estimates of the plasma voltage which are in reasonable agreement with the experimental values. The voltage appears to be fairly steady although some hysteresis is evident in the experimental voltage-versus-current curves.
2. The measured and theoretical values of the pressure do not agree, differing typically by as much as a factor of two. Substantial time-dependent behavior of the pressure is indicated from experimental pressure-versus-current traces. The time-dependent model, which accounts for the time variation of the current profile, predicts the correct trends in the non-stationary behavior of both the voltage and pressure, but the magnitude of the effects is significantly underestimated.
3. Calculations in which the flow is not assumed to be sonic at exit but, rather, the exit speed is determined by using the experimental value of the pressure, were also carried out.

Results of these calculations indicate slightly, but unconvincingly, better agreement with experimental voltage measurements than do calculations performed for the sonic condition.

Although we are reduced largely to speculation, we will now discuss a number of reasons which might contribute to the discrepancy between theory and experiment and suggest future improvements in both the models and experiments that could illuminate the subject further.

The first and most obvious limitation of using the model to compare with experimental results is the necessity of assuming some boundary condition concerning the exit velocity of the gaseous products. Fortunately, many of the plasma properties, such as its conductivity, do not depend strongly on this condition. One possibility for the nonsteady behavior of the capillary properties could be a rise in pressure in the brass extender tube, resulting in an unchoking of the flow as time progresses. Evidently, however, no such effect could account for the time-dependent voltage observed when capillaries are fired into open air, such as in the experiments done by Katulka, Burden, and White (1990), and other explanations must be investigated. One conceivable explanation could be the substantial amount of electrode ablation observed near the exit of capillary. This effect might be expected to lead to a situation in which the heavy, less mobile, electrode material prevents the escape of the capillary plasma. If such an effect does occur, it would become more dominant with increasing time since the ablation of metallic material will lag the ablation of polyethylene by a time period which depends very strongly on the temperature. This observation is consistent with the results. Electrode ablation could be included in the models discussed above, but the analysis would require the treatment of a nonhomogeneous mixture of polyethylene and the electrode material. We are currently attempting to develop such a model. Experimentally, the escape velocity of the gas at capillary exit could be measured. We have in fact attempted these measurements via use of fiber-optic cables placed close together near the tube exit. Measurements similar to these have been performed successfully in the past in the analysis of railgun plasma armatures (Zielinski and Powell 1990). For the cases investigated here, however, and particularly for the higher-current shots, the large magnitudes of the velocities involved have made the data difficult to evaluate. Much of the difficulty arises because the technique provides only distance-versus-time data and numerical differentiation, subject to significant error, is necessary to obtain the velocity. Preliminary results have suggested, however, that the exit velocities are considerably less than the local sound speed in the gas at the point in question. Further experimental work is required, however, before any quantitative statements can be made. It would also be worthwhile to undertake experiments with different types of electrode materials in an effort to determine the extent to which the electrodes affect the results.

A second reason for the lack of agreement between theory and experiment is the possi-

bility that the capillary plasma may be "contaminated." As indicated previously, this and other capillary-discharge models are based on the assumption that the capillary consists of a mixture of the various species which comprise the capillary wall. Clearly, however, if there is significant electrode erosion, whether at the breech or muzzle end of the discharge tube, the electrode material will become a part of the entrained plasma. The resulting mixture may then have properties different from those of the assumed mixture. Furthermore, particularly if the flow is not choked, there may be species diffusion from the region beyond the breech back into the capillary. Again, under this condition, the constituency assumed for the plasma will not be correct and its properties will be modified in some unknown way. We expect that this contamination may affect significantly sensitive plasma variables, such as the pressure, density, and velocity, but not insensitive ones such as the voltage or temperature.

A third possibility for the lack of agreement may be that the current is not being conducted throughout the entire radius of the capillary or, in other words, the thickness of the vapor zone may not be negligible as assumed. In his early experiments, Ibrahim (1980) found it necessary to postulate such an effect in order to achieve an energy balance between the radiated and dissipated power. Perhaps these or similar conclusions have been responsible for the development of a number of "two-zone" models such as proposed by Kovitya and Lowke (1984). In those models the vapor layer is treated as a region of finite thickness whose dimensions vary with the properties of the plasma in the central core. Necessarily, the treatment of the vapor layer is highly approximate and a number of assumptions, difficult to justify, are made concerning its properties. Nevertheless, the models discussed in this report could presumably be extended to two zones. It is evident that conduction of the current in a region having cross sectional area smaller than the tube itself, will produce higher pressures than for the case when the conduction occurs across the entire cross section. This aspect of the results would clearly be in better agreement with the experimental data. However, the two-zone models referred to above have all been steady state and are clearly not capable of explaining the time-dependent behavior of the pressure- or voltage-versus-time curves. An extension of those models to the time-dependent case would be necessary before one could hope to obtain any explanation of this aspect of the problem. Of course, the two-zone models are just a rough approximation to a real two-dimensional model. As pointed out in PZ1, a time-dependent, two-dimensional investigation of this problem is appropriate and timely. Experimentally, the radius of the current-carrying part of the capillary could probably be inferred from measurements of the magnetic-induction field as a function of radial distance in the tube. Somewhat similar experiments (Zielinski 1989b) have been performed in the past in railguns.

A fourth reason could be the experiment itself. Although the pressure transducer was

calibrated *in situ*, the time scale of the calibration was an order of magnitude greater than that of the experiment. Ordinarily, this difference would not be significant, but since a polyethylene wall shields the gage, the dynamic properties of the polyethylene may affect the results. In addition, it would be helpful to measure the pressure at a number of points along the length of the capillary, and for capillaries of fixed diameter.

A final reason that theory and experiment may not agree completely is that there may exist mechanisms, other than the thermal one assumed, which contribute to removal of wall material. Such mechanisms include, for example, pyrolysis and stress-wave effects which can cause spallation. These mechanisms, and the range of incident power densities for which they are important, have been discussed by Nemes and Randles (1989) and are important for these experiments.

8. REFERENCES

- Bennett, F. D., "Flow Fields Produced by Exploding Wires," in *Exploding Wires*. Edited by W. G. Chace and H. K. Moore. New York: Plenum, 1959, p.211.
- Burden, H. S. and D. D. Shear. "Transient Noise in Electronic Measurements." BRL-TR-1442, U. S Army Ballistic Research Laboratory, Aberdeen Proving Ground, MD, July 1969.
- Cambel, A. B. *Plasma Physics and Magnetofluidmechanics*. New York: McGraw-Hill, 1963, Chap. 6.
- Chrysomallis, G. S., C. D. Marinos, R. S. Ricci, and D. C. Cook. "Combustion Augmented Plasma Gun," in *Technology Efforts in ET Gun Propulsion*. Edited by A. A. Juhasz. U. S. Army Ballistic Research Laboratory, December 1988, Vol. I.
- Ebeling, W. and R. Sandig. "Theory of the Ionization Equilibrium in Dense Plasmas." *Ann. Physik*, vol. 28, p.289, 1973.
- Gilligan, J. G. and R. B. Mohanti. "Time-Dependent Numerical Simulation of Ablation-Controlled Arcs." *IEEE Trans. Plasma Sci.*, vol. PS-18, p.190, 1990.
- Gunther, K. and R. Radtke. *Electric Properties of Weakly Nonideal Plasmas*. Boston: Birkhauser, 1984.
- Holian, K. S., editor. *T-4 Handbook of Material Properties Data Bases*. Los Alamos: LA-10160-MS, 1984.
- Ibrahim, E. Z. "The Ablation Dominated Polymethylmethacrylate Arc." *J. Phys. D:Appl. Phys.*, vol. 13, p. 2045, 1980.
- Katulka, G. L., H. S. Burden, A. E. Zielinski, and K. J. White. "Electrical Energy Shaping for Ballistic Applications in Electrothermal Guns." *Proc. 27th JANNAF Combustion Meeting*, Cheyenne, WY, 1990 (in press). See also Ballistic Research Laboratory Report Number BRL-TR-3304, December 1991.
- Kempka, S. N. and D. A. Benson, informal presentation, Ballistic Research Laboratory, December 1991.
- Kovitya, P. and J. J. Lowke. "Theoretical Predictions of Ablation-Stabilised Arcs Confined in Cylindrical Tubes." *J. Phys. D: Appl. Phys.*, vol. 17, p. 1197, 1984.
- Lin, Shao-Chi. "Cylindrical Shock Waves Produced by Instantaneous Energy Release." *J. Appl. Phys.*, vol. 25, p. 54, 1954.
- Loeb, A. and Z. Kaplan. "A Theoretical Model for the Physical Processes in the Confined High Pressure Discharges of Electrothermal Launchers." *IEEE Trans. Magn.*, vol. MAG-25, p. 342, 1989.
- Mohanti, R. B., J. G. Gilligan, and M. A. Bourham. "Time-Dependent Simulation of Weakly Nonideal Plasmas in Electrothermal Launchers." *Phys. Fluids B*, vol. 13, p. 3046, 1991.
- Moore, C. E. "Atomic Energy Levels." Nat. Bur. Stand. U.S. Circ. No. 467, 1952.

- Nernes, J. A. and P. W. Randles. "Energy Deposition Phenomena in Partially Transparent Solids." *J. Thermophys. Heat Transfer*, vol. 3, p. 160, 1989.
- Niemeyer, L. "Evaporation Dominated High Current Arcs in Narrow Channels." *IEEE Trans. Power Appar. Syst.*, vol. PAS-97, p. 950, 1978.
- Pizer, S. M. *Numerical Computing and Mathematical Analysis*. Chicago: Science Research Associates, 1975, Chap. 3.
- Powell, J. D. and A. E. Zielinski. "Analysis of the Plasma Discharge in an Electrothermal Gun." in *Technology Efforts in ET Gun Propulsion*. Edited by A. A. Juhasz. U. S. Army Ballistic Research Laboratory, December 1989, Vol. II.
- Rolader, G. E. and J. H. Batteh. "Thermodynamic and Electrical Properties of Railgun Plasma Armatures." *IEEE Trans. Plasma Sci.*, vol. PS-17, p. 439, 1989.
- Ruchti, C. B. and L. Niemeyer. "Ablation Controlled Arcs." *IEEE Trans. Plasma Sci.*, vol. PS-14, p. 423, 1986.
- Spitzer, L. *Physics of Fully Ionized Gases*. New York: Interscience Publishers, 1965, Chap. 5.
- Tidman, D. A. and S. A. Goldstein. "Thermal Transport to Hypervelocity Gun Tubes by High Pressure Partially Ionized Gas Flows." GTD 85-4, GT Devices, Alexandria, VA, 1985.
- Tidman, D. A., Y. C. Thio, S. A. Goldstein, and D. S. Spicer. "High Velocity Electrothermal Mass Launchers." GTD 86-7, GT Devices, Alexandria, VA, 1986.
- VonNeumann, J. and R. D. Richtmyer. "A Method for the Numerical Calculation of Shocks." *J. Appl. Phys.*, vol. 21, p. 232, 1950.
- Zeldovich, Y. B. and Y. P. Raizer. *Physics of Shock Waves and High-Temperature Hydrodynamic Phenomena*. New York: Academic, 1966, Vol. I, Chap. III.
- Zielinski, A. E. "BRL Pulsed Power Facilities and Research Status." Paper presented at the Sixth Electromagnetic Launcher Association Meeting, Eglin AFB, FL, May 1989.
- Zielinski, A. E. "BRL Pulsed Power Facilities and Research Status." Paper presented at the Seventh Electromagnetic Launcher Association Meeting, Milpitas, CA, December 1989.
- Zielinski, A. E. and J. D. Powell. "Plasma Analysis of a Small-Bore, Arc-Armature Railgun." BRL-TR-3175, U. S. Army Ballistic Research Laboratory, Aberdeen Proving Ground, MD, November 1990.
- Zollweg, R. J. and R. W. Liebermann. "Electrical Conductivity of Nonideal Plasmas." *J. Appl. Phys.*, vol. 62, p. 3621, 1987.

<u>No. of</u> <u>Copies</u>	<u>Organization</u>	<u>No. of</u> <u>Copies</u>	<u>Organization</u>
2	Administrator Defense Technical Info Center ATTN: DTIC-DDA Cameron Station Alexandria, VA 22304-6145	1	Commander U.S. Army Tank-Automotive Command ATTN: ASQNC-TAC-DIT (Technical Information Center) Warren, MI 48397-5000
1	Commander U.S. Army Materiel Command ATTN: AMCAM 5001 Eisenhower Ave. Alexandria, VA 22333-0001	1	Director U.S. Army TRADOC Analysis Command ATTN: ATRC-WSR White Sands Missile Range, NM 88002-5502
1	Commander U.S. Army Laboratory Command ATTN: AMSLC-DL 2800 Powder Mill Rd. Adelphi, MD 20783-1145	1	Commandant U.S. Army Field Artillery School ATTN: ATSF-CSI Ft. Sill, OK 73503-5000
2	Commander U.S. Army Armament Research, Development, and Engineering Center ATTN: SMCAR-IMI-I Picatinny Arsenal, NJ 07806-5000	2	Commandant U.S. Army Infantry School ATTN: ATZB-SC, System Safety Fort Benning, GA 31903-5000
2	Commander U.S. Army Armament Research, Development, and Engineering Center ATTN: SMCAR-TDC Picatinny Arsenal, NJ 07806-5000	(Class. only) 1	Commandant U.S. Army Infantry School ATTN: ATSH-CD (Security Mgr.) Fort Benning, GA 31905-5660
1	Director Benet Weapons Laboratory U.S. Army Armament Research, Development, and Engineering Center ATTN: SMCAR-CCB-TL Watervliet, NY 12189-4050	(Unclass. only) 1	Commandant U.S. Army Infantry School ATTN: ATSH-CD-CSO-OR Fort Benning, GA 31905-5660
(Unclass. only) 1	Commander U.S. Army Rock Island Arsenal ATTN: SMCRI-TL/Technical Library Rock Island, IL 61299-5000	1	WL/MNOI Eglin AFB, FL 32542-5000 <u>Aberdeen Proving Ground</u>
1	Director U.S. Army Aviation Research and Technology Activity ATTN: SAVRT-R (Library) M/S 219-3 Ames Research Center Moffett Field, CA 94035-1000	2	Dir, USAMSAA ATTN: AMXSY-D AMXSY-MP, H. Cohen
1	Commander U.S. Army Missile Command ATTN: AMSMI-RD-CS-R (DOC) Redstone Arsenal, AL 35898-5010	1	Cdr, USATECOM ATTN: AMSTE-TC
		3	Cdr, CRDEC, AMCCOM ATTN: SMCCR-RSP-A SMCCR-MU SMCCR-MSI
		1	Dir, VLAMO ATTN: AMSLC-VL-D
		10	Dir, USABRL ATTN: SLCBR-DD-T

<u>No. of Copies</u>	<u>Organization</u>	<u>No. of Copies</u>	<u>Organization</u>
1	Defense Nuclear Agency ATTN: Dr. R. Rohr 6801 Telegraph Road Alexandria, Virginia 22310	1	Director Benet Weapons Laboratory U. S. Army Armament Research, Development, and Engineering Center ATTN: SMCAR-CCB-RA, Dr. Garry Carofano Watervliet, NY 12189
3	Commander U. S. Army Armament Research, Development, and Engineering Center ATTN: SMCAR-FSA-E, Dr. Thadeus Gora Mr. John Bennett Mr. Al Graf Picatinny Arsenal, NJ 07806-5000	1	Director DARPA ATTN: Dr. Peter Kemmeyer 1400 Wilson Boulevard Arlington, VA 22209
2	Commander U. S. Army Armament Research, Development, and Engineering Center ATTN: SMCAR-CCL-FA, Mr. Harry Moore Mr. Henry Kalin Picatinny Arsenal, NJ 07806-5000	1	Commander SDIO ATTN: SDIO/IST, MAJ M. Huebschman Washington, DC 20301-7100
3	Commander U. S. Army Armament Research, Development, and Engineering Center ATTN: SMCAR-AEE-B, Bldg. 382 Mr. Donald Chiu Dr. David Downs Dr. Lee Harris Picatinny Arsenal, NJ 07806-5000	1	Director U. S. Army Research Office ATTN: Dr. Mikael Cifan P. O. Box 12211 Research Triangle Park, NC 27709-2211
2	Commander U. S. Army Armament Research, Development, and Engineering Center Electric Armaments Program Office (EAPO) ATTN: SMCAR-FSC, Bldg. 329 Annex Mr. Gregory Ferdinand Mr. William Morelli Fire Support Armaments Center Picatinny Arsenal, NJ 07806-5000	1	Department of the Navy Naval Sea Systems Command ATTN: CDR Craig Dampier CSEA 06 KR12 Washington, DC 20362-5101
		1	Director Naval Research Laboratory ATTN: Dr. Andrew Moskovitch Code 4730 Washington, DC 20375-5000
1	Director Benet Weapons Laboratory U. S. Army Armament Research, Development, and Engineering Center ATTN: SMCAR-CCB-RM, Dr. Pat Vottis Watervliet, NY 12189	1	WL/MNSH EM Launcher Technology Branch ATTN: Mr. Donald Littrell Hypervelocity Research Complex Wright Laboratory/Armament Directorate Eglin Air Force Base, FL 32542-5434
		1	Director Sandia National Laboratories Advanced Projects Division, Org. 9123 ATTN: Dr. David Benson Albuquerque, NM 87185-5800

<u>No. of Copies</u>	<u>Organization</u>	<u>No. of Copies</u>	<u>Organization</u>
1	Director Sandia National Laboratories Advanced Projects V ATTN: Dr. Steve Kempka Albuquerque, NM 87185-5800	2	IAP Research, Inc. ATTN: Dr. John P. Barber Mr. David P. Bauer 2763 Culver Avenue Dayton, OH 45429-3723
2	Director Sandia National Laboratories Energetic Materials Division, Org. 8357 ATTN: Dr. Steven Vosen Dr. Robert Armstrong Livermore, CA 94551-0969	2	Maxwell Laboratories ATTN: Dr. Ian McNab Dr. Mark Wilkinson 8888 Balboa Avenue San Diego, CA 92123
1	Alliant Techsystems, Inc. ATTN: Dr. Jim Kennedy MN 48-2300 7225 Northland Drive Brooklyn Park, MN 55428	1	Olin Ordnance ATTN: Dr. Hugh A. McElroy 10101 9th Street North St. Petersburg, FL 33716
1	FMC Corporation Naval Systems Division M170 ATTN: Dr. David Cook 4800 East River Road Minneapolis, MN 55421-1498	1	Pacific-Sierra Research Corp. ATTN: Dr. Gene E. McClellan 1401 Wilson Boulevard Arlington, Virginia 22209
3	FMC Corporation Northern Ordnance Division M170 ATTN: Dr. Anthony Giovanetti Dr. Gene Johnson Dr. Jahn Dyvik 4800 East River Road Minneapolis, MN 55421-1498	1	Paul Gough Associates, Inc. ATTN: Dr. Paul S. Gough 1048 South Street Portsmouth, NH 03801
2	General Dynamics Land Systems Division ATTN: Dr. Melvin Widner Dr. Bruce van Duesen MZ 436-21-14 P. O. Box 2074 Warren, MI 48090-2074	1	Princeton Combustion Research Laboratory ATTN: Dr. N. A. Messine 4275 US Highway One North Monmouth Junction, NJ 08852
4	GT-Devices, Inc. ATTN: Dr. J. Robert Grieg Dr. Derek Tidman Dr. Shyke Goldstein Dr. Niels Windsor 5705A General Washington Drive Alexandria, VA 22312	2	Science Applications International Corporation ATTN: Dr. Keith A. Jamison Dr. Glenn E. Rolader 1247-B North Eglin Parkway Shalimar, FL 32579
		3	Science Applications International Corporation ATTN: Dr. Sanford Dash Dr. Ashwin Hosangadi Dr. Neeraj Sinha 501 Office Center Drive, Suite 420 Fort Washington, PA 19034-3211

<u>No. of Copies</u>	<u>Organization</u>	<u>No. of Copies</u>	<u>Organization</u>
2	Science Applications International Corporation 1 ATTN: Dr. C. C. Hsiao Dr. Gary Phillips 10210 Campus Point Drive San Diego, CA 92121		State University of New York at Buffalo Department of Electrical Engineering ATTN: Dr. W. J. Sarjeant 312 Bonner ECL-SUNY/AB Buffalo, NY 14260
2	Science Applications International Corporation 2 ATTN: Dr. Jad H. Batteh Mr. Lindsey D. Thornhill 1503 Johnson Ferry Road, Suite 100 Marietta, GA 30062		University of Tennessee Space Institute Center for Laser Applications, MS-14 ATTN: Dr. Dennis R. Keefer Mr. Roger Crawford Tullahoma, TN 37388-8897
1	S Cubed Division of Maxwell Labs ATTN: Dr. Eduardo Waisman 3398 Carmel Mountain Road San Diego, CA 92121	2	University of Texas Center for Electromechanics Balcones Research Center ATTN: Mr. William Weldon Mr. Raymond Zaworka 10100 Burnet Road, Bldg. 133 Austin, TX 78758
2	SPARTA Inc. ATTN: Mr. Jeffrey Kezerian Dr. Michael M. Holland 9455 Towne Center Drive San Diego, CA 92121-1964	1	The University of Texas at Austin Institute for Advanced Technology ATTN: Dr. Harry D. Fair 10100 Burnet Road Austin, TX 78758
1	Supercon Inc. ATTN: Mr. Charles Renaud 830 Boston Turnpike Road Shrewsbury, MA 01545		
1	Auburn University ATTN: Dr. Raymond F. Askew Leach Nuclear Science Center Auburn University, AL 36849-3501		
1	Auburn University ATTN: Dr. Eugene Clothiaux 206 Allison Lab Auburn University, AL 36849-5311		
3	North Carolina State University Department of Nuclear Engineering ATTN: Dr. Mohamed Bourham Dr. John Gilligan Dr. Orlando Hankins Box 7909 Raleigh, NC 27695-7909		
1	The Pennsylvania State University Propulsion Engineering Research Center Mechanical Engineering Department ATTN: Dr. Kenneth K. Kuo 140 Research Building "E" University Park, PA 16802		

USER EVALUATION SHEET/CHANGE OF ADDRESS

This laboratory undertakes a continuing effort to improve the quality of the reports it publishes. Your comments/answers below will aid us in our efforts.

1. Does this report satisfy a need? (Comment on purpose, related project, or other area of interest for which the report will be used.) _____

2. How, specifically, is the report being used? (Information source, design data, procedure, source of ideas, etc.) _____

3. Has the information in this report led to any quantitative savings as far as man-hours or dollars saved, operating costs avoided, or efficiencies achieved, etc? If so, please elaborate. _____

4. General Comments. What do you think should be changed to improve future reports? (Indicate changes to organization, technical content, format, etc.) _____

BRL Report Number BRL-TR-3355 Division Symbol _____

Check here if desire to be removed from distribution list. _____

Check here for address change. _____

Current address: Organization _____
Address _____

DEPARTMENT OF THE ARMY
Director
U.S. Army Ballistic Research Laboratory
ATTN: SLCBR-DD-T
Aberdeen Proving Ground, MD 21005-5066

OFFICIAL BUSINESS

BUSINESS REPLY MAIL

FIRST CLASS PERMIT No 0001, APG, MD

Postage will be paid by addressee

Director
U.S. Army Ballistic Research Laboratory
ATTN: SLCBR-DD-T
Aberdeen Proving Ground, MD 21005-5066



NO POSTAGE
NECESSARY
IF MAILED
IN THE
UNITED STATES

